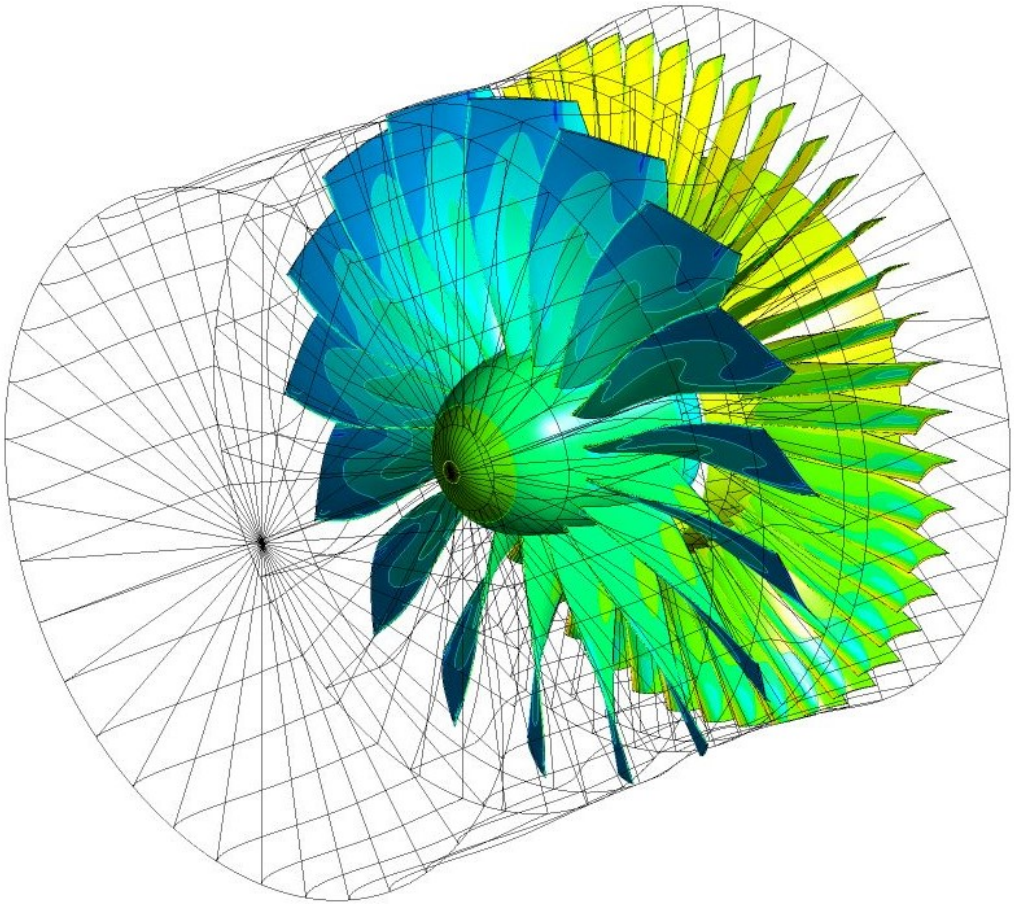

Aerothermal performance of fan outlet guide vanes in modern geared turbofan engines

Master's thesis in Applied Mechanics and Sustainable Energy Systems

ALBIN BJÖRKMAN
PAUDAN HASSAN MAHAVEER

DEPARTMENT OF MECHANICS AND MARITIME SCIENCE
CHALMERS UNIVERSITY OF TECHNOLOGY
Gothenburg, Sweden 2021
www.chalmers.se

Master's thesis 2021:48

Aerothermal performance of fan outlet guide vanes in modern geared turbofan engines

Albin Björkman
Paudan Hassan Mahaveer

CHALMERS
UNIVERSITY OF TECHNOLOGY

Department of Mechanics and Maritime Science
Division of Fluid Dynamics
Chalmers University of Technology
Gothenburg, Sweden 2021

Aerothermal performance of fan outlet guide vanes in modern geared turbofan engines

Supervisor: Oliver Sjögren, Department of Mechanics and Maritime Science
Examiner: Carlos Xisto, Department of Mechanics and Maritime Science

Master's Thesis 2021:48
Department of Mechanics and Maritime Science
Division of Fluid Mechanics
Chalmers University of Technology
SE-412 96 Gothenburg
Telephone +46 31 772 1000

Cover: Total pressure contour of the hub and blades of a ultra high bypass ratio geared turbofan.

Typeset in LaTeX
Printed by Chalmers Reproservice
Gothenburg, Sweden 2021

Abstract

In the process of making aero engines more energy efficient, hybrid electrical concepts with electrical generators at the core of the engine are being explored. This brings additional challenges to the engine architecture. This thesis will focus on exploring the possibility of cooling these electrical generators using already existing surfaces in the engine. In particular, the possibility of using the fan outlet guide vanes (OGV) as heat sinks. Two different sets of OGV are tested, in additional to the original set for the engine, a low aspect ratio OGV of larger size with lower blade count is investigated. The proposed idea is to have pipes transport a cooling fluid from the generator to the OGV in order to cool down the generator. The requirement on this cooling system is the ability to reject 20 kW of heat at a minimum pressure drop in the pipes. This problem is tackled by doing CFD RANS simulations on the low pressure section of the aero engine, consisting of the outer and inner end walls of the engine, together with the turbofan and OGV. As aircraft operate at different conditions, these have to be considered in running the simulations. The operating conditions tested in this thesis is cruise, when the aircraft is traveling at a high velocity at a high altitude, and idle, when the airplane is stationary on the ground with the engine running at a low speed. These simulations are run using the k - ω SST turbulence model along with the γ - θ turbulence transition model, and the object of the simulations is to capture the factors that contribute to heat rejection, namely heat transfer coefficient on the OGV and mass flow though the engine.

This data is then used together with theoretical and empirical data to design a piping system going through the OGV. The design of the piping system is not based on simulation data, and standard fluid mechanics and heat transfer equations are used to estimate the possible heat rejection for a certain pipe configuration. With these two connected, a optimization code based on the genetic algorithm is used to create multiple optimal piping configurations by maximising heat rejection and minimising pressure drop. The piping parameters used is number of pipe passes, distance between pipes, and first pipe location in the OGV. An additional parameter is used containing a number of different coolants, to determine the most suitable candidate. The result of this is a Pareto front, containing data to design a piping system based required heat rejection to give minimal pressure drop. In the idle case, where it is most difficult to meet the requirement, the heat rejection possibilities range from 20 - 120 kW, with a required pumping power of 10^{-1} - 10^{2} W. For the low count OGV, the heat rejection is in range 20 - 100 kW and pressure drop ranges from 10^{-2} - 10^{2} W.

Keywords: CFD, RANS, SST, OGV Heat transfer, HTC, Cooling system, Turbofan engine, Fan OGV, Low aspect ratio OGV

Acknowledgements

I would like to thank Carlos Xisto for his supervision and input over the course of the thesis. His input and knowledge of the subject has been invaluable, keeping us on the right track.

I would also like to thank Marcus Lejon for his feedback and assistance with the fan simulations. Without his help this thesis would have taken much longer time.

Finally, I would like to thank my partner Nora Enggren, for her emotional support during hectic periods and her continuous encouragement during this process.

Albin Björkman, Gothenburg, June 2021

I would like to thank Carlos Xisto for providing an opportunity to work on this project and for all his advice, guidance and immense support throughout the entirety of the thesis. He was always there to provide his knowledge and assistance whenever complications were faced, without which this project would be way harder to complete.

I also want to express much appreciation to Marcus Lejon, Oliver Sjögren and Isak Jonsson for their excellent suggestions and guidance throughout the project.

Lastly, I would like to thank all my friends who in various ways contributed directly and indirectly not just in my studies but the time spent here at Chalmers University of Technology.

Paudan Hassan Mahaveer, Gothenburg, June 2021

Contents

List of Figures

List of Tables

Nomenclature

$\dot{m}$	Mass flow
η_p	Polytropic efficiency
$\gamma - \theta$	Transitional turbulence model
γ	thermal capacity ratio
μ	Viscosity
ν_t	Turbulent viscosity
$\overline{a}$	Time averaged quantity a
ρ	Density
σ_k	Turbulent Prandtl number for k
σ_ϵ	Turbulent Prandtl number for ϵ
σ_ω	Turbulent Prandtl number for ω
τ_w	Wall shear stress
$\tilde{a}$	Favré averaged quantity a
a'	Fluctuation of property a
c_p	Specific heat capacity
$k - \epsilon$	Turbulence model
$k - \omega$	Turbulence model
k	Thermal conductivity
p	Static pressure
p_0	Total pressure
P_k	Modelled production term for k
Pr	Prandtl number
R	Ideal gas constant
R_{wall}	Wall resistance
Re	Reynolds number
Re_{xt}	Transitional Reynolds number
S	Specific entropy
s_{ij}	Strain rate tensor
SM	Surge Margin
T	Static temperature
T_w	Wall static temperature
T_{ref}	Reference static temperature
Tu	Freestream turbulence intensity
u^*	Friction velocity
u^+	Non dimensional velocity
u_i	velocity component
V	Absolute velocity

y	Distance from the wall
y^+	Non dimensional wall distance
τ_{ij}	Viscous stress tensor
BPR	By Pass Ratio
e_0	Specific total energy
FPR	Fan Pressure Ratio
h	Specific enthalpy
HPC	High Pressure Compressor
HTC	Heat Transfer Coefficient
IPC	Intermediate Pressure Compressor
LPC	Low Pressure Compressor
OGV	Outlet Guide Vane
q	Heat flux
SST	Shear stress transport

1
Introduction

1.1 Background

Since the 1950s, the interest in commercial aviation has risen continually, showing in the ever growing number of flights per year. The number of flights between 2004 and 2019 increased by over 60%[9]. While the rapid growth of interest in aviation has led to large improvements in aviation and engine technology, it is difficult to keep up. In the year 2018, aviation accounted for 2.4% of global carbon dioxide emissions from fossil fuels. It is predicted to increase threefold by the year 2050, constituting 25% of global carbon dioxide budget proposed by the Paris climate agreement. Goals set up by the International Air Transport Association to limit this is to have a non increasing CO2 emissions after the year 2020, and to reduce aviation CO2 net emissions by 50% (relative to levels in 2005) in the year 2050[8].

In effort to reduce the environmental effect of aviation, major focus have been placed on designing and developing more electrical aircraft. An aircraft consists of a large number of sub-systems, of varying importance. Some of these systems, such as the cabin pressurization, flight control systems and communication systems, are vital to the operation of the aircraft, while some are more for comfort, such as air conditioning and electrical power for entertainment purposes. All of these systems needs some sort of power to function, and is generally based on one of three different sources, electrical power, hydraulic power, or pneumatic power. With an increasing number of sub-systems installed in modern aircraft, together with the desire to electrify the pneumatic and hydraulic systems, the aircraft electrical consumption is bound to increase. In addition to being more environmentally friendly, more electric aircraft are expected to be more reliable and having better maintainability, making them even more desirable[22].

1.1.1 Power generators

The power used for all systems in the aircraft origin from the engines. The pneumatic and hydraulic power comes from bleeding air from the engine compressors. The electrical power comes from an radial shaft connected to the high pressure shaft. The change to more electric aircraft and overall increase in demand for electricity creates the need for larger electrical generators. Mounting these larger generators in the conventional way however becomes troublesome. Larger generators require more space, are heavier, and required a thicker and heavier shaft. An idea is proposed to

instead have the generator at the engine core, mounted directly on the high pressure shaft. Not only could save space, but it is also expected reduce fuel consumption, and cost of aircraft[23]. However, this bring in additional challenges with respect to engine architecture, installation weight and heat management.

1.1.2 Generator cooling

Electric generators produce a large amount of heat during its operation and hence there is a need to constantly cool the internal components to make sure that the generator is not damaged and operates safely. Common ways to cool conventional generators is by using heat exchangers to reject generator heat into cold bleed air from the compressors or into cold jet fuel from the engine[24]. This is however not very practical for an electrical generator at the engine core. Instead, a new type of cooling system is needed.

1.2 Problem Description

The aim of this thesis is to investigate the concept of using existing turbomachinery surfaces to reject heat generated by an electrical generator at the engine core. The surface in particular that will be investigated is the aerothermal properties of the Fan-OGV (Outlet Guide Vane), provided by our industrial partner GKN Aerospace in the framework of an ongoing project. The project aim is to establish the aerothermal performance of the OGV, and to design the inner cooling circuit that deliver the required heat exchanger performance of 20 kW heat rejection with minimum pressure losses.

This cooling circuit will go from the generator at the engine core, out through the OGV, and back to the core again. This concept is illustrated in Figure 1.1. In addition, two sets of OGV will be investigated. The regular OGV (Fan - OGV1 in the figure) and a low aspect ratio OGV (Fan - OGV2).

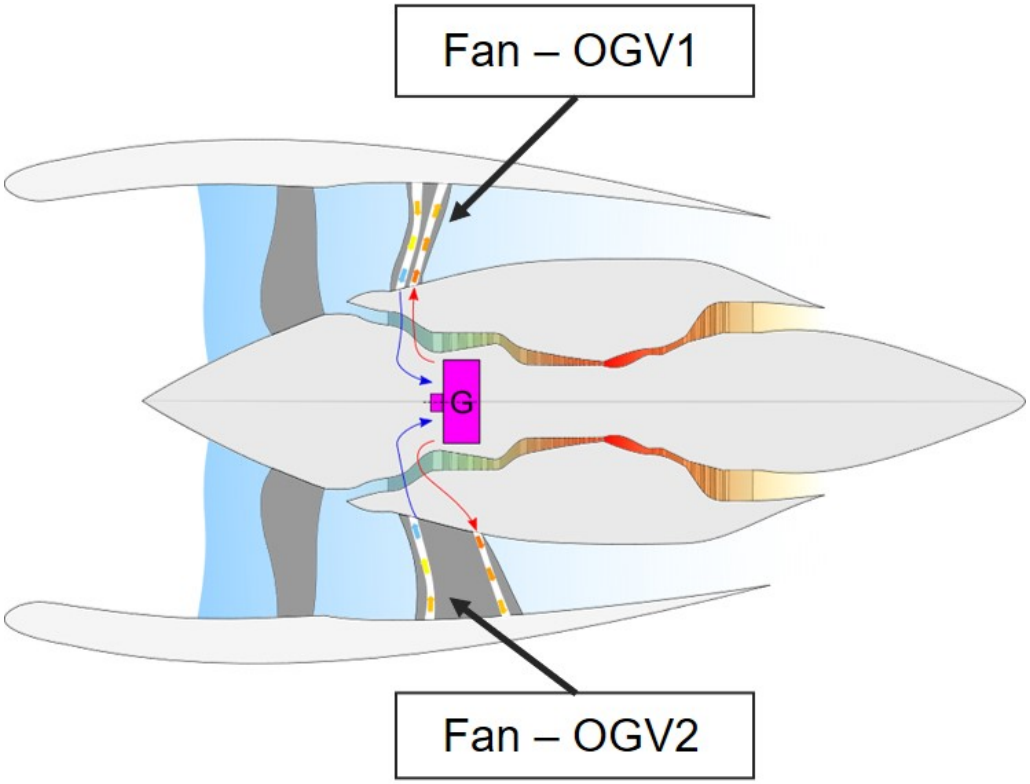

Figure 1.1: A concept of an aero engine with heat sinks in the OGV.

In addition to designing the most optimal cooling circuit for the OGV, different possible coolants will also be investigated. These are given in Table 1.1, along with their relevant properties. Here, ρ is density, c_p is specific heat capacity, μ is dynamic viscosity, and k is thermal conductivity.

	ρ [kg/m^3]	c_p [kJ/kg·K]	μ [mPa·s]	k [W/m·K]
Dowtherm J	806.2	2.0708	0.4267	0.1125
Paratherm LR	706.8	2.2920	0.5132	0.1455
Therminol D12	706.8	2.3918	0.4343	0.0975
Syltherm XLT	778.4	1.9289	0.5362	0.0938
50% Ethylene Glycol	1018.1	3.6547	0.7953	0.3956
60% Ethylene Glycol	1028.0	3.4888	0.9400	0.3562
70% Ethylene Glycol	1036.9	3.3130	1.1000	0.3213
80% Ethylene Glycol	1045.1	3.1266	1.4000	0.2893
90% Ethylene Glycol	1053.1	2.9255	1.8000	0.2607
100% Ethylene Glycol	1062.1	2.7011	2.2000	0.2396

Table 1.1: A list of coolants used in design of the cooling system.

1.3 Scope of work

The flow of around the OGV external surface, that is the flow through the engine, is modelled with CFD RANS simulations. The performance in cruise will be evaluated

and compared to an earlier iteration of the engine. Two different operating points, cruise and ground idle, will be considered and evaluated. For the low aspect ratio OGV, only the ground idle will be considered.

The flow in the inner cooling channels is modelled through correlations based on literature. To calculate the wall thermal resistivity a simplified 2 dimensional model will be derived by curve fitting in-house 2D heat conduction computational results. Two different possible materials for the OGV will be concidered, one high conductivity aluminium alloy, and one low conductivity titanium alloy. These results will be connected in MATLAB. Further, the piping system will be designed using an optimization algorithm, based on the genetic algorithm.

2

Theory

2.1 Turbomachinery

Machines used to transfer energy between a rotating component and a fluid are called turbomachines. These can broadly be categorized into two types of machines. First machines which transfer energy to a fluid, such as pumps, compressors, and fans. Second, machines that extract energy from a fluid, such as gas turbines, steam turbines, and hydraulic turbines. Furthermore turbomachinery can be categorized by the nature of the flow path through the device. When the flow is parallel to the axis of rotation, it is called axial flow. When the flow undergoes a 90° turn in relation to the rotational axis, it is called radial flow. The nature and application of these two types of machines differs quite substantially, and as most aero engines use axial flow machines, only these will be considered further. Compressors and turbines generally consists of a section of rotating blades called a rotor, and a section of stationary blades called a stator. Together these form a stage.

Most of todays aircraft are driven by some sort of turbomachine. Fighter jets are driven by low bypass turbofan engines, helicopters are driven by turboshaft engines, smaller aircraft are driven by turboprop engines, and large commercial aircraft are driven by the high bypass turbofan engine. The high bypass turbofan engine will be in focus for this thesis.

A turbofan engine operates based on the Joule - Brayton cycle and generally consists of a fan, multiple compressors followed by a combustion chamber, and multiple turbines. The Joule - Brayton cycle is shown in Figure 2.1 and is an ideal thermodynamic cycle based on isentropic compression of the working fluid (1 - 2), followed by an isobaric temperature increase (2 - 3) and lastly an isentropic expansion (3 - 4)[5].

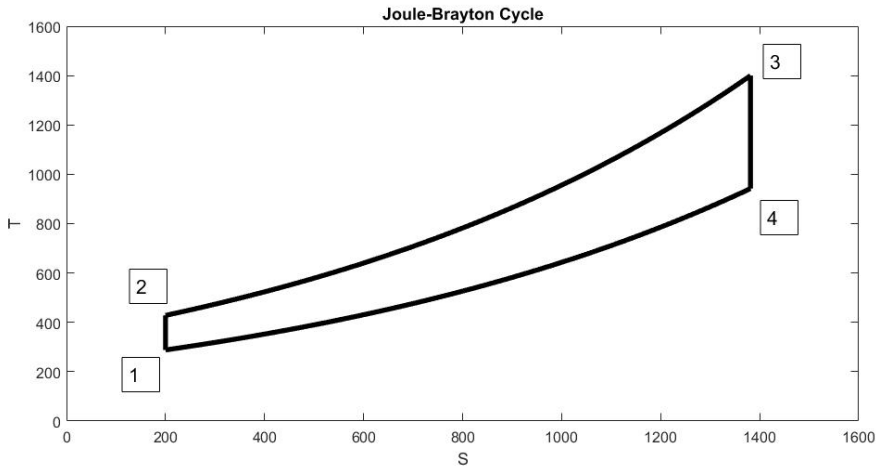

Figure 2.1: The Joule - Brayton ideal thermodynamic cycle based on isentropic compression, isobaric heating, and isentropic expansion

The equations that are utilized for this simple model are

$$\frac{p_2}{p_1} = \left(\frac{T_2}{T_1}\right)^{\frac{\gamma}{\gamma-1}} \tag{2.1}$$

$$Tds = c_p dT \tag{2.2}$$

where the first equation describes an isentropic relation between temperature T and pressure p, where γ is the thermal capacity ratio of the working fluid. The second equation relates the change in entropy s with the variation in temperature where c_p is the specific heat capacity. The energy added to or taken from the fluid can be given by the variation in specific entalphy, defined by

$$\Delta h = c_p \Delta T \tag{2.3}$$

The pressure ratio for the compression is equal to the expansion. Due to the high expansion temperature in stage 3, more energy can be extracted than is required for the compression. In a turbofan, this cycle is implemented by compression from a fan and multiple compressors, a temperature increase from combustion, and expansion through multiple turbines. A basic schematic of a turbo fan is shown in Figure 2.2.

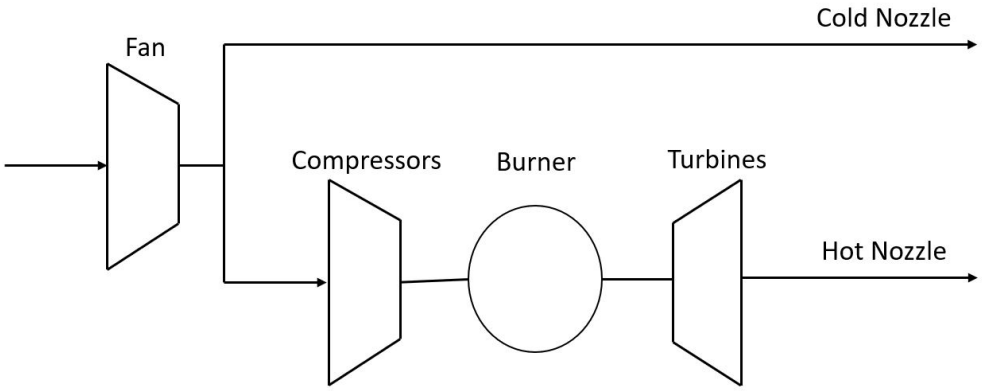

Figure 2.2: Schematic of fluid flow through a turbofan engine.

The thrust is generated by the cold jet from the cold nozzle (passing through only the fan) and the hot jet from the hot nozzle (passing through the core). The ratio of mass flow of these two jets is called the Bypass Ratio (BPR). The air entering the core is compressed and slowed down, before entering the combustion chamber where it is mixed with jet fuel and ignited to increase temperature at a constant pressure. The hot high pressure gas is then expanded through the turbines. Going through the compressors, the air pressure is gradually increased, and the compressors need to increase in rotational speed.

Because of this, the compressors are mounted on different shafts to allow for a varied rotational speed. In general, two or three shafts are used. One for the Low Pressure Compressors (LPC) closest to the fan, one for the High Pressure Compressors (HPC) closest to the burner, and sometimes one for the Intermediate Pressure Compressors (IPC) in the middle. A similar division is done in the turbine section, as the high pressure turbines can rotate faster than the intermediate or low pressure turbines closer to the nozzle. The turbines are used to power the compressors, and this is achieved by having the high pressure turbines share a shaft with the high pressure compressors, and the same for the intermediate and low pressure systems. After the turbines the flow is further expanded in the exit nozzle and converted into thrust.

2.1.1 Fan

Since this thesis mainly focuses on the fan section of the engine, no more attention will be paid to the remaining sections. In Figure 2.3, the fan and surrounding geometry is shown.

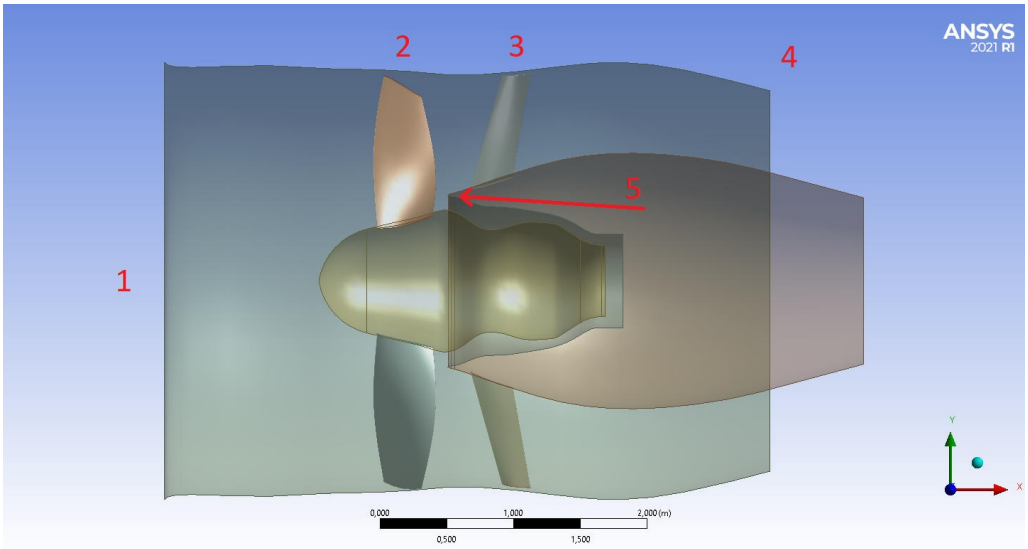

Figure 2.3: Sections of the fan.

The fan consists of a row of rotor blades (number 2 in Figure 2.3) and a row of stator blades (number 3). The rotor blades will transfer energy to the fluid by increasing the total pressure. The increase in total pressure is called the Fan Pressure Ratio (FPR), measured as

$$\text{FPR} = \frac{p_{02}}{p_{01}} \tag{2.4}$$

Where P_{02} is the total pressure measured after the rotor blades and P_{01} (number 1) is the total pressure measured at the fan face. Normally, P_{02} is measured after the stator (number 4), but in this thesis only the rotor pressure ratio will be considered to keep in line with previous work on the same turbofan engine. This performance metric generally depends on three different parameters, the rotational speed of the fan, the axial velocity, and the fluid deflection in the blades. The stator row, also called Outlet Guide Vanes (OGV), are responsible for diffusing the flow, reducing the velocity and increasing static pressure, as well as de-swirling the flow (reducing velocity in the rotational direction). In between these blade rows a splitter lip (number 5) is located responsible for guiding a small portion of the flow into the core of the engine and the rest through the OGV.

In turbomachinery, compressor and fan off-design performance are shown in compressor maps. These maps are constructed by measuring the pressure ratio and mass flow at different operating conditions while keeping rotational speed constant, forming a speed line. The speed line's upper limit is choke, where the velocity reaches speed of sound in the entire passage and higher mass flow is impossible. The lower limit is given by surge, this can happen when the flow on one or more blades separate at the leading edge, causing the blades to stall. Surging is unsteady and causes the compressor to oscillate between stalled and un-stalled behaviour.

In between these extremes, a design point can be established to have a safety margin to surge. The surge margin SM for the design point is given by

$$SM = \left(\frac{\dot{m}_{dp}}{\dot{m}_{limit}} \frac{\mathrm{FPR}_{limit}}{\mathrm{FPR}_{dp}} - 1 \right) \cdot 100 \tag{2.5}$$

where $\dot{m}_{dp}$ and $\dot{m}_{limit}$ are the mass flow in the design point and surge point respectively, and same notation for fan pressure ratio. Furthermore, an operating line can be constructed by varying the rotational speed and deciding a design point for each rotational speed. How this is done is up to the compressor designer, common approaches is to use either the point of highest efficiency or a constant surge margin on each speed line[7]. In Figure 2.4 an example of a pressure map for a fan can be seen.

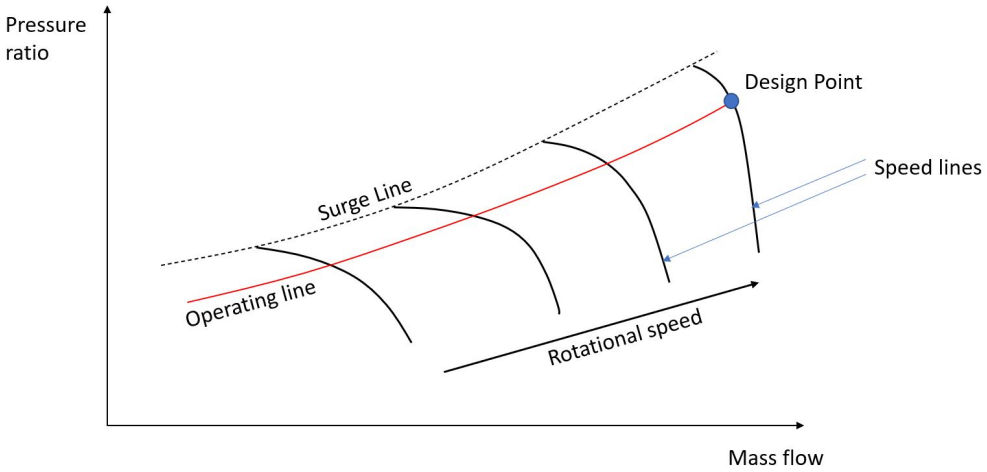

Figure 2.4: Pressure map for a compressor or fan.

Also worth considering is that the efficiency of the fan behaves in similar ways to the pressure ratio, meaning that when the flow is choked and the pressure ratio is low, the efficiency is also low. In this work, the efficiency is measured by the compressor polytropic efficiency, which is given by the ratio between the incremental ideal enthalpy change to the corresponding actual enthalpy variation.

$$\eta_p = \frac{dh_{is}}{dh} \tag{2.6}$$

or

$$\frac{T_2}{T_1} = \left(\frac{P_2}{P_1} \right)^{\frac{\gamma - 1}{\eta_p \gamma}} \tag{2.7}$$

2.2 Computational Fluid dynamics

In the following section, the aspects of computational fluid dynamics (CFD) modelling will be discussed along with the used solver Ansys CFX.

2.2.1 Governing equations

The basics of all types of CFD solvers are the Navier-Stokes equations, which is a set of differential equation describing the the transport of mass, momentum, and energy. The first of these is the continuity equation, which is based on the conservation of mass on a fluid element. Second is the momentum equation, based around Newton's second law formulated on a fluid element. The last equation, responsible for the variation of energy, based on the first law of thermodynamics, is called the energy equation. These equations are given below in compact form using index notation. Index notation is based around free and summation indices. Free indices appear once in an expression and means that

$$a_i = \begin{bmatrix} a_x \\ a_y \\ a_z \end{bmatrix} \tag{2.8}$$

Summation indices appear twice and means that

$$a_i b_i = a_x b_x + a_y b_y + a_z b_z \tag{2.9}$$

The Navier-Stokes equations, ignoring source terms appearing on the right side of the equation, are

$$\frac{\partial Q}{\partial t} + \frac{\partial F_j}{\partial x_j} = 0 \tag{2.10}$$

Where Q is the state vector defined as

$$Q = \begin{bmatrix} \rho \\ \rho u_i \\ \rho e_0 \end{bmatrix} \tag{2.11}$$

and F is the flux vector

$$F = \begin{bmatrix} \rho u_j \\ \rho u_i u_j + p\delta_{ij} - \tau_{ij} \\ \rho u_j e_0 + u_j p + q_j - u_i \tau_{ij} \end{bmatrix}. \tag{2.12}$$

In these equations, ρ is the fluid density u_i is a velocity component, and τ_{ij} is the viscous stress tensor defined as

$$\tau_{ij} = 2\mu s_{ij} - \frac{2}{3}\mu \frac{\partial u_k}{\partial x_k}\delta_{ij} \tag{2.13}$$

where μ is the viscosity, and s_{ij} the strain rate tensor is defined as

$$s_{ij} = \frac{1}{2}\left(\frac{\partial u_i}{\partial x_j} + \frac{\partial u_j}{\partial x_i}\right). \tag{2.14}$$

e_0 is the specific total energy, given by the sum of internal and kinetic energy as

$$e_0 = e + \frac{1}{2}u_{ii}, \tag{2.15}$$

and q is the heat flux. To solve these equations, equations of state are needed that relates certain properties of the fluid to one another. In this case, the model used is the ideal gas law, formulated as

$$p = \rho RT \tag{2.16}$$

$$dh = c_p dT \tag{2.17}$$

$$c_p = c_p(T) \tag{2.18}$$

where R is the ideal gas constant. If the system has large variations of temperature or composition (in case of multiphase flow), c_p is calculated as function of the temperature, otherwise this can be taken as a constant[3].

2.2.2 Turbulence

Turbulent flow in turbomachinery (and in general) is almost always present. It is characterized by flow irregularities, high diffusivity and high dissipation. Because of its irregularity, all turbulent flows will have a transient solution. These phenomena appear on a very wide range of scales, and are incredibly difficult to resolve properly using a computational method. This issue has given rise to a method of time averaging the flow equations defined by decomposing a quantity as

$$a_i = \overline{a_i} + a_i' \tag{2.19}$$

where $\overline{a_i}$ is the time averaged quantity and a_i' is a fluctuation for any property a. The time average is defined as

$$\overline{a_i} = \frac{1}{2T}\int_{-T}^{T} a_i dt. \tag{2.20}$$

A method used when the turbulent flows is also compressible is Favré averaging, in which the time average is weighted by density. This is defined as

$$\widetilde{a_i} = \frac{\overline{\rho a_i}}{\overline{\rho}} \tag{2.21}$$

Using Favré average, the total quantity a is defined again by its averaged and fluctuating parts

$$a_i = \widetilde{a_i} + a_i'' \tag{2.22}$$

Note that $a' \neq a''$. Using these simplifications, we have removed the need to resolve all turbulent scales, and also given ourselves the option to solve an inherently unsteady flow using a steady method, yielding the mean field as solution. This method of time averaging is called Reynolds averaging, and when applied to the governing flow equations we end up with the Reynolds Averaged Navier-Stokes equations, often called RANS equations. When the Favré average is used, the equation set is called the Favré Averaged Navier Stokes (FANS) equations.

2.2.3 Turbulence equations

The FANS equations are given as follows, again on a compact form using index notation. Note that for simplicity source terms are omitted in the momentum and energy equations[6].

$$\frac{\partial Q}{\partial t} + \frac{\partial F_j}{\partial x_j} = 0 \tag{2.23}$$

$$Q = \begin{bmatrix} \bar{\rho} \\ \bar{\rho}\tilde{u}_i \\ \bar{\rho}\tilde{e_0} \end{bmatrix} \tag{2.24}$$

$$F = \begin{bmatrix} \bar{\rho}\tilde{u}_j \\ \bar{\rho}\tilde{u}_i\tilde{u}_j + \bar{p} + \overline{\rho u_i'' u_j''} - \overline{\tau_{ij}} \\ \bar{\rho}\tilde{u}_j\tilde{e_0} + \tilde{u}_j\bar{p} + \overline{u_j''p} + \overline{\rho u_j'' e_0''} + \overline{q_j} - \overline{u_i\tau_{ij}} \end{bmatrix} \tag{2.25}$$

2.2.4 Turbulence Model

The process of averaging the governing equations give rise to additional terms, such as the Reynolds stress tensor $\overline{u_i'' u_j''}$. These are difficult to describe analytically and must be modelled. A multitude of different modelling approaches exist for turbulent flow, each with its own strengths and weaknesses. Generally, it's a trade off between accuracy and computational resources, and this will be a major factor in picking a suitable turbulence model. One common approach is to use the Boussinesq assumption, in which the Reynolds stress is modelled using the turbulent viscosity. Hence, one can formulate the the diffusion terms (losses due to viscous effects) in the momentum equation as follows. For simplicity's sake, this is shown for a incompressible fluid using Reynolds average instead of Favré average.

$$\frac{\partial}{\partial x_j}\left[\nu\left(\frac{\partial \bar{u_i}}{\partial x_j} + \frac{\partial \bar{u_j}}{\partial x_i}\right) - \overline{u_i' u_j'}\right] = \frac{\partial}{\partial x_j}\left[(\nu + \nu_t)\left(\frac{\partial \bar{u_i}}{\partial x_j} + \frac{\partial \bar{u_j}}{\partial x_i}\right)\right] \tag{2.26}$$

A similar procedure can be done for the terms in the energy equation to obtain a turbulent thermal diffusitivity. Further, the turbulent viscosity can be calculated in multiple ways. Again, a common method is using a two equation model, in which the turbulent viscosity is calculated using two variables as

$$\nu_t = c_\mu \frac{k^2}{\epsilon} = \frac{k}{\omega} \tag{2.27}$$

where k is the turbulent kinetic energy, ϵ the turbulent dissipation, ω the specific turbulent dissipation rate, and c_μ a constant. As can be seen, one only need two of these three variables to obtain the turbulent viscosity. The turbulent kinetic energy, and one of the two others. These are the so called $k-\epsilon$ and $k-\omega$ models[17][16]. These variables are calculated from their respective differential equation, which are derived from the Navier-Stokes equations. In the exact versions of these equation, multiple new unknowns appear, similar to what happens when the Navier-Stokes

equations are averaged. Therefore it is common practice to use modelled equations for k, ω, and ϵ. The modelled k equation is given as

$$\frac{\partial \bar{\rho}\tilde{k}}{\partial t} + \frac{\partial}{\partial x_j}\left[\bar{\rho}\tilde{k}\tilde{u_j} - \left(\mu + \frac{\mu_t}{\sigma_k}\right)\frac{\partial \tilde{k}}{\partial x_j}\right] = P_k - \bar{\rho}\tilde{\epsilon} \tag{2.28}$$

where P_k is the modelled production term, and σ_k is the turbulent Prandtl number for k. The modelled differential equation for ϵ is

$$\frac{\partial \bar{\rho}\tilde{\epsilon}}{\partial t} + \frac{\partial}{\partial x_j}\left[\bar{\rho}\tilde{\epsilon}\tilde{u_j} - \left(\mu + \frac{\mu_t}{\sigma_\epsilon}\right)\frac{\partial \tilde{\epsilon}}{\partial x_j}\right] = \frac{\tilde{\epsilon}}{\tilde{k}}\left(c_{\epsilon 1}P_k - c_{\epsilon 2}\bar{\rho}\tilde{\epsilon}\right) \tag{2.29}$$

where σ_ϵ is the turbulent Prandtl number for ϵ, and c_ϵ are two constants. For ω, the modelled equation is

$$\frac{\partial \bar{\rho}\tilde{\omega}}{\partial t} + \frac{\partial}{\partial x_j}\left[\bar{\rho}\tilde{\omega}\tilde{u_j} - \left(\mu + \frac{\mu_t}{\sigma_\omega}\right)\frac{\partial \tilde{\omega}}{\partial x_j}\right] = \frac{\tilde{\omega}}{\tilde{k}}\left(c_{\omega 1}P_k - c_{\omega 2}\bar{\rho}\tilde{k}\tilde{\omega}\right) \tag{2.30}$$

where σ_ω is the turbulent Prandtl number for ω, and $c_{\omega 1}$ and $c_{\omega 2}$ are constants. In this present work, the turbulence model used will be the $k-\omega$ SST (Shear Stress Transport)[15]. This is a combination of the $k-\epsilon$ and the $k-\omega$ turbulence models. The main feature of the SST model is that it implements a $k-\omega$ model in the inner boundary layer and a $k-\epsilon$ model in the outer boundary layer and the core flow. This is done to cover up for the weaknesses of the individual turbulence models. The $k-\epsilon$ model has two main weaknesses, it over predicts shear stress in adverse pressure gradient flows, and wall functions are needed to model the boundary layer. These two issues are solved by the $k-\omega$ model, which is good at solving adverse pressure gradient flows, and does not require the usage of wall functions, instead resolving the boundary layer down to the wall. The disadvantage of the $k-\omega$ model is that it is less accurate far from the wall[1]. This combination is achieved by formulating the specific dissipation rate ω in terms of the the turbulent kinetic energy k and the turbulent dissipation ϵ as

$$\omega = \frac{\epsilon}{c_\mu k}. \tag{2.31}$$

By doing this, the transport equation for ϵ can be expressed in terms of ω.

$$\frac{\partial \bar{\rho}\tilde{\omega}}{\partial t} + \frac{\partial}{\partial x_j}\left[\bar{\rho}\tilde{\omega}\tilde{u_j} - \left(\mu + \frac{\mu_t}{\sigma_\omega}\right)\frac{\partial \tilde{\omega}}{\partial x_j}\right] = \alpha\frac{P_k}{\mu_t} - \beta\bar{\rho}\tilde{\omega}^2 + \frac{2}{\tilde{\omega}}(1-F_1)\sigma_{\omega 2}\frac{\partial \tilde{k}}{\partial x_i}\frac{\partial \tilde{\omega}}{\partial x_i} \tag{2.32}$$

In this equation, F_1 is a transition function that is equal to 1 near the wall and 0 far from the wall. All constants in the function are on the form

$$\alpha = (1-F_1)\alpha_{k-\epsilon} + F_1\alpha_{k-\omega} \tag{2.33}$$

such that they smoothly transactions from values used for $k-\omega$ model to values used for $k-\epsilon$ model as wall distance increases[2].

2.2.4.1 Transitional turbulence model

The model used to predict the transition from laminar to turbulent flow is the $\gamma - \theta$ transitional turbulence model[18]. In addition to the transport equations already in use, this model introduces two new transport equations, one for the intermittency and one for the transition onset criteria in terms of momentum thickness Reynolds number. Because of the two extra transport equations, a solution is expected to require around 18 % additional computing time[4]. However, for compressor blades with a Reynolds number of around 10^6, the expected fraction of laminar flow is 0.38, based on the Mayle empirical correlation for transitional onset[19].

$$\frac{Re_{xt}}{Re} = \frac{380000\,(100Tu)^{-\frac{4}{5}}}{(\rho/\mu)VL_{device}} \tag{2.34}$$

Where Re_{xt} is the transitional Reynolds number, Re is the Reynolds number, L_{device} is the length of the component, and Tu is the freestream turbulence intensity, calculated from the turbulent kinetic energy k as

$$Tu = \frac{(2k/3)^{0.5}}{V} \tag{2.35}$$

where V is the absolute velocity. In the current case it is expected to have Reynolds number of around $1.5 \cdot 10^6$ at the OGV inlet in cruise, and as such a large portion of laminar flow is expected. As a consequence of this, a transitional turbulence model is deemed necessary and will be used for all design point simulations.

2.2.5 Wall treatment

The region closest to a wall is called the boundary layer. In this region large velocity gradients can be expected since at the wall velocity is zero. The boundary layer is divided up in two regions, the inner and the outer. The inner region closest to the wall is dominated by viscous forces and the outer region is dominated by turbulent diffusion. Distances in the boundary layer is measured by

$$y^+ = \frac{\rho u^* y}{\mu} \tag{2.36}$$

where y is the distance from the wall and u^* is the friction velocity defined as

$$u^* = \sqrt{\frac{\tau_w}{\rho}} \tag{2.37}$$

where τ_w is the wall shear stress defined as

$$\tau_w = \mu \left(\frac{\partial u}{\partial y}\right)_{y=0} \tag{2.38}$$

The inner region is defined by $y^+ < 5$ while the outer as $y^+ > 30$. In between these is a transition region that shares characteristics from both these regions. A typical appearance of the boundary layer is shown in Figure 2.5.

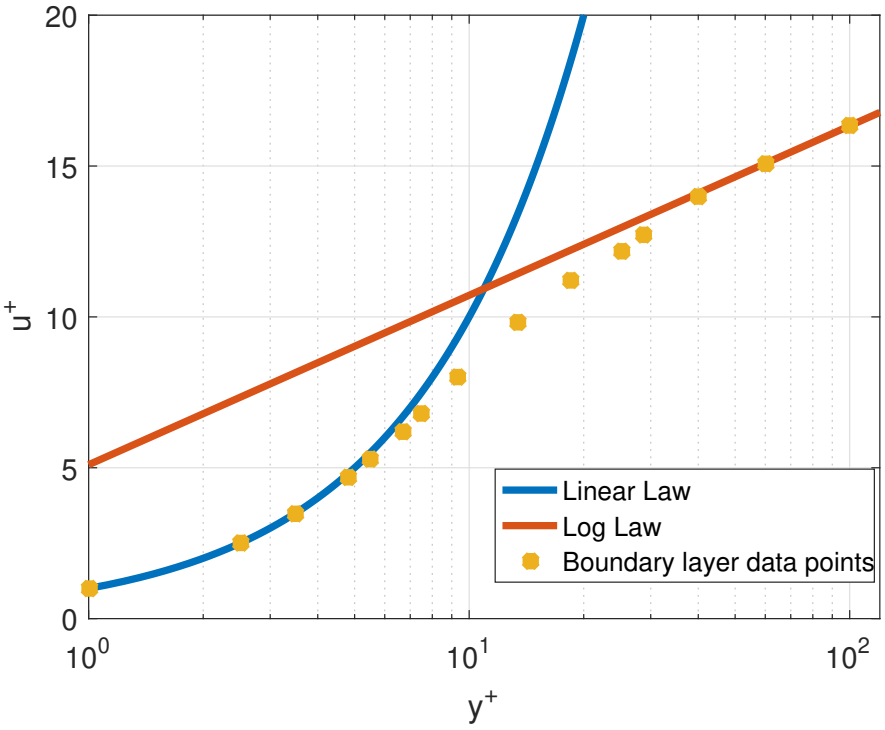

Figure 2.5: Law of the wall

The inner region is mathematically defined by the linear law

$$u^+ = y^+ \tag{2.39}$$

where u^+ is a non dimensional velocity

$$u^+ = \frac{u}{u^*}. \tag{2.40}$$

The outer region is defined by the logarithmic law

$$u^+ = \frac{1}{\kappa} ln(y^+) + B \tag{2.41}$$

where κ and B are constants values 0.41 and 5, respectively. In modelling of the boundary layer, two approaches are commonly used. Either wall functions are used, in the $k - \epsilon$ for example. This method uses the assumption that the boundary flow behaves like a turbulent boundary layer, and uses grid points in the outer regions to approximate the whole boundary layer. This method has the advantage that the inner boundary layer doesn't need to be resolved, and a coarse grid can be used.

The other method, used in $k - \omega$ and $k - \omega$ SST models, is to resolve the the

inner boundary layer and modify the turbulence models to fit the particular nature of the boundary layer. This method uses many more grid points close to the wall and is thus more computationally heavy. But in cases where for instance the thermal properties are of importance, it is in general requirement to resolve the boundary layer instead of modeling it, since heat transfer at the wall is very important for the temperature field of the whole domain. The temperature boundary layer is modelled using the thermal law of the wall[21]. The non dimensional temperature T^+ is modelled by blending the viscous sublayer (first half of equation 2.42) and the logarithmic law of the wall (second half of equation 2.42).

$$T^+ = Pr \cdot y^* \cdot e^{-\Gamma} + [2.12ln(y^*) + \beta]\, e^{-1/\Gamma} \tag{2.42}$$

where

$$\beta = \left(3.85Pr^{1/3} - 1.3\right)^2 + 2.12ln(Pr) \tag{2.43}$$

$$\Gamma = \frac{0.01(Pr \cdot y^*)^4}{1 + 5Pr^3 y^*} \tag{2.44}$$

$$Pr = \frac{\mu c_p}{k}. \tag{2.45}$$

Here, k is the thermal conductivity. The heat flux in the boundary layer is given by

$$q = \frac{\rho c_p u^*}{T^+}(T_w - T_{ref}) \tag{2.46}$$

Where T_w is the wall temperature and T_{ref} is the reference temperature, in the the CFD code specified as the wall adjacent element temperature[4].

2.3 Heat transfer

Heat transfer can be defined as the flow of heat (thermal energy) due to a temperature difference between material bodies. The rate of heat transfer is dependent on the temperature difference between the bodies, larger the difference, larger will be the rate of heat transfer. The heat travelling from one body to another is also affected by the resistance to heat flow, offered by the medium through which it passes. The general rate equation can be expressed as,

$$\text{rate of heat transfer } = \text{temperature difference/heat flow resistance}$$

During the heat transfer process the temperatures may change and this would cause change in rate of heat transfer as well, and is called unsteady state heat transfer. When the temperatures do not change, it is called steady state heat transfer. Heat can be transferred by various mechanisms, commonly referred as modes, such as conduction, convection and radiation.

2.3.1 Conduction

Conduction involves heat transfer by the interaction of neighbouring molecules having different energy contents. It can be described as the transfer of molecular energy between solids or stationary fluids, from the most energetic particles to the

neighbouring particles with less energy. For example, consider steady state heat conduction as shown in Figure 2.6. A plane wall with its end faces maintained at different temperatures, such that $T_1 > T_2$. This difference in temperature causes the transfer of heat in the positive x-direction. The rate of heat transfer through the wall can be measured, which depends on the thickness dx, area A, the wall material and temperature difference across the wall.

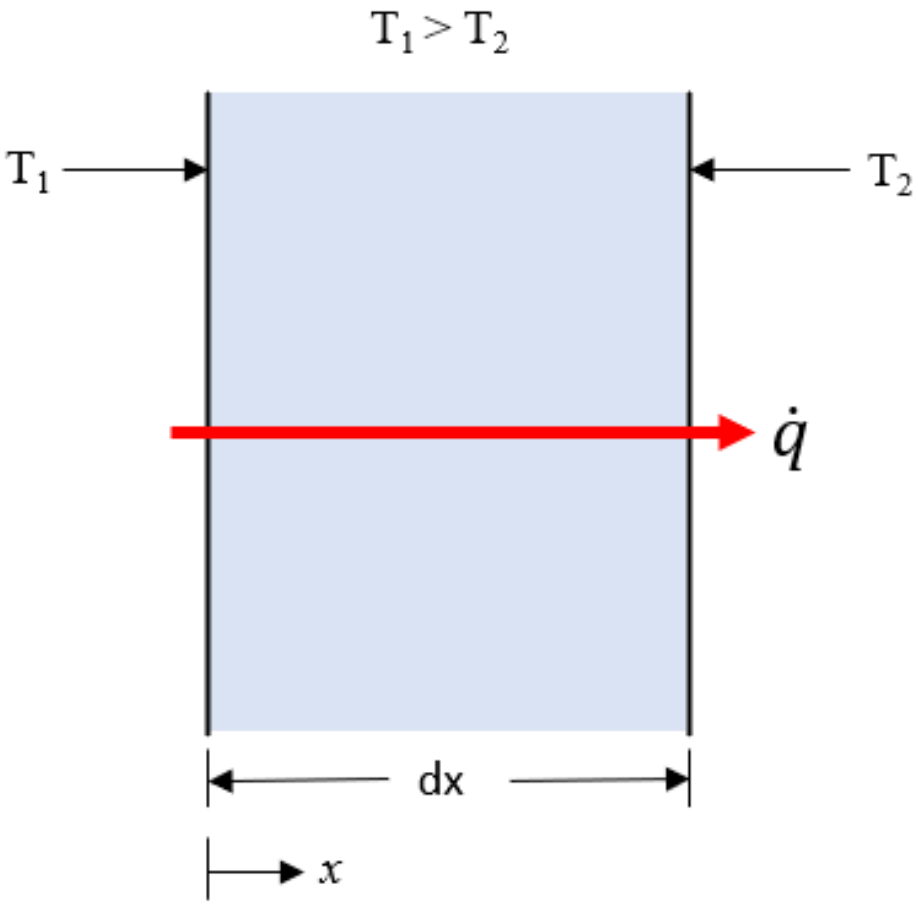

Figure 2.6: Conduction heat transfer mode.

The mathematical description of heat conduction is based on Fourier's law, for the one-dimensional plane wall, the rate equation is expressed as,

$$\dot{q}_i = -k\frac{\partial T}{\partial x_i} \tag{2.47}$$

where heat flux $\dot{q}$ (W/m^2) is the heat transfer conducted per unit area perpendicular to the direction of transfer and k(W/mK) is the physical parameter of the medium known as coefficient of thermal conductivity. The minus sign indicates that heat flows from a hotter body to a colder body, that is, in the direction of negative temperature gradient. For a two-dimensional steady state heat conduction, the finite differenced heat equation is given as,

$$\frac{\partial^2 T}{\partial x^2} + \frac{\partial^2 T}{\partial y^2} + \frac{\dot{q}}{k} = 0 \tag{2.48}$$

2.3.2 Radiation

Radiation is the transfer of energy by electromagnetic waves. Heat transfer by radiation is often neglected and is only significant when the temperature differences are greater. Heat transfer model in this thesis include conduction and convection. Radiation is not taken into account.

2.3.3 Convection

Convective heat transfer occurs when there is a temperature gradient between a surface and a moving fluid. It involves two mechanisms, energy transfer due to random molecular motion and macroscopic motion of the fluid. Consider the flow of fluid over a hot plate as shown in Figure 2.7.

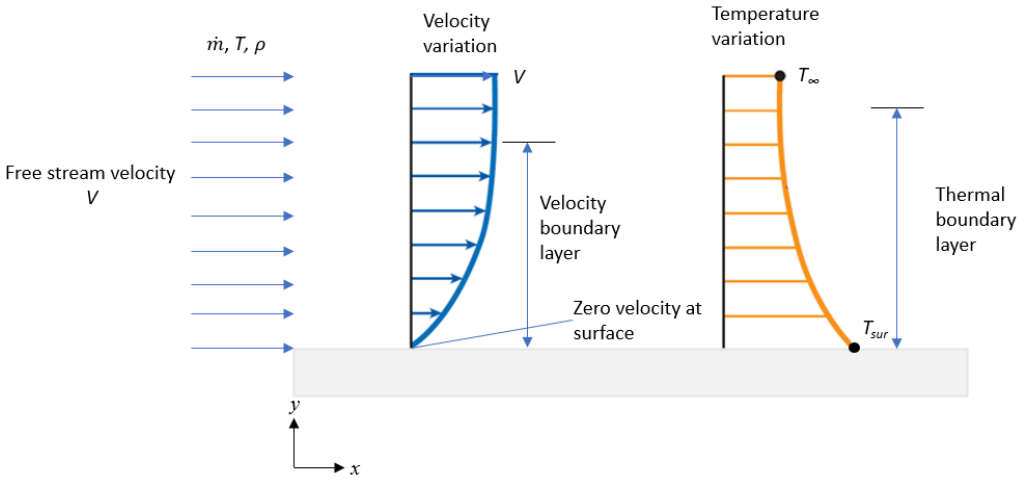

Figure 2.7: Heat transfer from hot plate to fluid by convection.

The fluid-surface interaction leads to the development of a region called velocity boundary layer. Where the velocity varies from zero at the surface to free stream velocity of the flow. At the leading edge, the temperature distribution of the fluid is uniform and as it makes contact with the plate, thermal equilibrium is reached between the fluid and the plate. These fluid particles exchange energy with the adjacent fluid layer and gives rise to temperature gradient in the fluid as seen in Figure 2.7. This region where temperature gradient exist is called thermal boundary layer. Heat is first transferred from the plate to the adjoining fluid layer by conduction. The heat conducted into this layer is then carried away from the surface by convection and is finally transferred to the fluid outside the boundary layer.

The flow of fluid can be natural or by force. When the flow is driven by density changes due to temperature variations in the fluid, it is called free or natural convection. When the fluid movement is maintained by supplying the required quantity

of mechanical energy from an external source, for example a pump or a fan, it is called forced convection.
The flow of fluid can also be classified according to the geometry of conduit as external flow and internal flow. The external flow is the unbounded flow of fluid over a surface, i.e, the boundary layers develop freely without external constraints and is surrounded by a free flow region in which velocity and temperature gradients are negligible. Foe example, fluid flow over a flat plate as shown above in Figure 2.7 and flow over curved surfaces like sphere, cylinder, airfoil are considered as external flow. On the other hand, internal flow is such a flow in which the fluid is completely confined by a surface, such as flow through pipes or ducts. When the fluid makes contact with the inner surface of the pipe the velocity varies from zero at the wall to a maximum value at the pipe center, i.e, as the fluid flows the boundary layer develops and finally merges at the centreline.

The rate equation for convective heat transfer can be expressed using Newton's law of cooling,

$$\dot{q} = h(T_{surf} - T_{\infty}) \tag{2.49}$$

where $\dot{q}$ (W/m^2) is the convective heat flux, T_{surf} is the surface temperature and T_{∞} is the static temperature outside the thermal boundary layer and h(W/m^{2}K) is the convection heat transfer coefficient. In the above equation the relation between the amount of heat transferred and temperature gradient is linear. Whereas, the heat transfer coefficient h is influenced by factors like the boundary layer form, geometry and fluid properties. Therefore, determination of the heat transfer coefficient is crucial and has significant influence on the amount of heat transferred.

Heat transfer coefficient h may be expressed in terms of Nusselt number. The most common non-dimensional parameters relevant to heat transfer, follow:

Nusselt number

The Nusselt number is the ratio of convection to conduction heat transfer across a boundary. It is non-dimensional heat transfer coefficient. Since convection includes diffusion and advection, if Nu = 1, then it would mean the fluid is stationary and all the heat transfer is by conduction and higher Nusselt number mean that the fluid motion enhances the heat transfer by advection.

$$Nu = \frac{hL}{k} \tag{2.50}$$

where h is the heat transfer coefficient, L is the characteristic length and k is the thermal conductivity.

Reynolds number

The Reynolds number is defined as the ratio of inertia forces and viscous forces that influence behaviour of flow in the boundary layer. It provides information on

whether the flow is laminar or turbulent. At low Reynolds number, the viscous forces are dominant and the flow tends to be laminar. When the Reynolds number is large, inertia forces dominate and the flow tends to be turbulent. The mixing of the fluid in turbulent flow increases heat transfer between the fluid particles, which in turn increases the convective heat transfer coefficient.

$$Re = \frac{\rho u L}{\mu} \tag{2.51}$$

where ρ, u and μ are density, average velocity and dynamic viscosity of the fluid respectively, and L is the characteristic length.

Prandtl number

The Prandtl number is the ratio of momentum diffusivity to thermal diffusivity. It is related to velocity boundary layer thickness and thermal boundary layer thickness.

$$Pr = \frac{\mu c_p}{k} \tag{2.52}$$

where μ, c_p and k are dynamic viscosity, specific heat and thermal conductivity of the fluid respectively. Note that there is no length scale accounted and is dependent only on the property of fluid.
These non-dimensional groups are quite useful in the representation of results and correlations of experimental data.

2.4 Heat exchangers

The transfer of heat between two fluids at different temperatures is an essential part in many engineering applications for heating or cooling purposes. The device used to achieve this heat transfer is called heat exchanger. The applications of heat exchangers is very broad and among them the notably common applications are their use in refrigeration, heating and air conditioning systems, chemical industries, food processing industries, power production and district heating in large plants, etc. Heat exchangers are usually classified according to the heat transfer process, flow arrangement, construction type and heat transfer mechanisms. Heat transfer in heat exchangers can occur by direct contact of the fluids or indirectly through a wall that separates the fluids from mixing. For most of the heat exchangers that are employed, heat transfer occurs indirectly. Heat is transferred from the hot fluid to the inner wall by convection, through the inner wall to outer wall by conduction and from the wall to the cold fluid by convection.
Based on flow arrangement heat exchangers can be classified as parallel-flow, counter-flow and cross-flow heat exchangers. In parallel-flow, the fluids enter and leave the heat exchanger in the same direction as shown in Figure 2.8(a). In counter-flow arrangement, the fluids enter the heat exchanger at opposite ends and flow in opposite directions as seen in Figure 2.8(b) . In cross-flow arrangement, the fluids flow perpendicular to each other and the flow can be unmixed or mixed as illustrated in Figure 2.9.

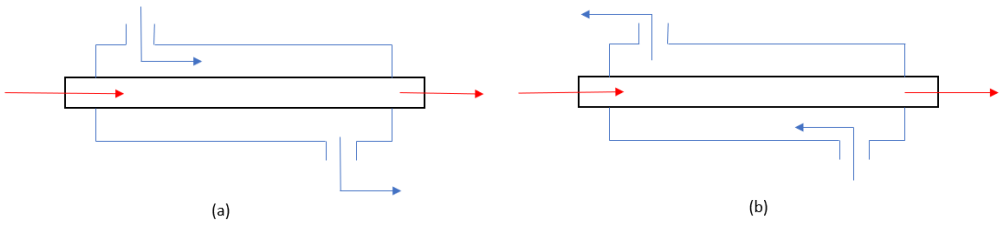

Figure 2.8: (a) Parallel flow. (b) Counter flow

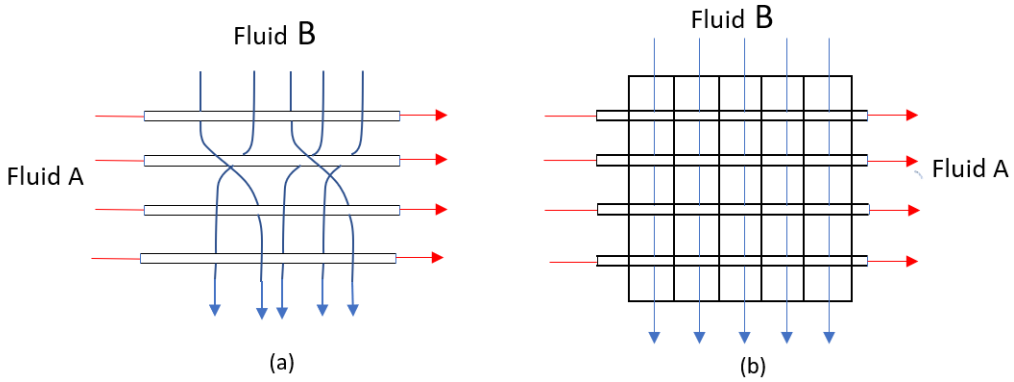

Figure 2.9: Cross flow heat exchangers. (a)Stream A unmixed, stream B mixed. (b)Both streams unmixed

The flow is said to be unmixed when there are separate channels over the tubes to prevent the fluid from flowing in the transverse direction. When the fluid is free to move in the transverse direction the flow is said to be mixed. Cross flow arrangement is usually present in compact heat exchangers where there is strict constraint on the weight and volume of the heat exchanger[13]. A good heat exchanger design is the one that meets the required heat load performance with minimum pressure losses.

2.4.1 The overall heat transfer coefficient

The overall heat transfer coefficient is a measure of combined ability of conduction and convection resistances to heat transfer between fluids separated by wall. It is an essential parameter used for the calculation of heat transfer in heat exchangers. It can be expressed as,

$$\frac{1}{UA} = \frac{1}{h_o A_o} + R_{wall} + \frac{1}{h_i A_i} \tag{2.53}$$

where U is the overall heat transfer coefficient, h_o is the external heat transfer coefficient, h_i is the internal heat transfer coefficient, A_o is the external surface area, A_i is the internal surface area and R_{wall} is the wall resistance.

2.4.2 Wall resistance

Wall resistance or thermal resistance is the resistance offered by the material to flow of heat. Similar to how electric resistance is related with the conduction of electricity, thermal resistance is related with the conduction of heat. The heat flow through a wall is dependent on the temperature difference across it, thermal conductivity of the material and thickness of the wall. The thermal resistance is directly proportional to the thickness of the wall and inversely proportional to the wall conductivity. It may be defined as the ratio of temperature difference between the two faces of the material (driving potential) to the rate of heat transfer.

$$R_{wall} = \frac{\Delta T}{\dot{q}} \tag{2.54}$$

2.4.3 Internal pressure drop

When fluid flows through pipe, energy losses are bound to happen. One of the main sources of pressure drop is due to the friction that arise between the pipe wall and the fluid. Frictional effects also arise within the fluid based on the viscosity of the fluid. Apart from the frictional loss, pressure drop also occur from so called minor losses due to pipe fittings, entrance and exit of pipe, sudden expansion or contraction and bends. Minor losses result from rapid changes in the direction or magnitude of the velocity of fluid[]. The basic approach to evaluate energy loss in a pipe system is by using the Bernoulli's equation,

$$\left[\frac{P}{\rho g} + \frac{v^2}{2g} + z\right]_{in} = \left[\frac{P}{\rho g} + \frac{v^2}{2g} + z\right]_{out} + h_L \tag{2.55}$$

where $\frac{P}{\rho g}$, $\frac{v^2}{2g}$ and z are pressure head, velocity head and potential head respectively, and h_L is the total head loss.

2.5 Coolant

Coolant is used to regulate the temperature of the generator by keeping it at the desired temperature. It collects and transports the heat from the generator and rejects the heat to the incoming air in the engine through the heat exchanger that is integrated in the fan OGV. In order to transfer the heat efficiently, it is important for the coolant to have low viscosity, high thermal conductivity and high specific heat. It also has to have high operating temperatures, needs to be environmentally friendly, non-corrosive and safe. Furthermore, since electrical components are involved, coolant has to have low electrical conductivity.

There are different types of coolants like water, mineral-based and synthetic coolants. Water is non-toxic, has high specific heat and low viscosity but relatively low boiling point and high freezing point. Mineral based coolants are obtained from crude oil. They have higher viscosity and lower specific heat compared to water. Mineral

based oil can be categorised into three different types determined by the chemical bond as naphthenic, parrafinic and aromatic. Synthetic fluids are manmade coolants. They have high operating temperature and long service life but expensive compared to mineral oils. Popular fluid types include polyalphaolefins (POA), synthetic esters(SE) and poly alkylene glycols(PAG).

3
Methods

3.1 Geometry

The geometry used is provided by GKN aerospace, and consists of the low pressure section of the engine, meaning the fan and the LPC. The baseline geometry for the model was created as part of the NFFP6 project VINK. For this current MSc project, the LPC section of the model is unimportant and is omitted. The fan and OGV geometry, where the number of blades is 17 and 43 respectively, is presented in Figure 3.1.

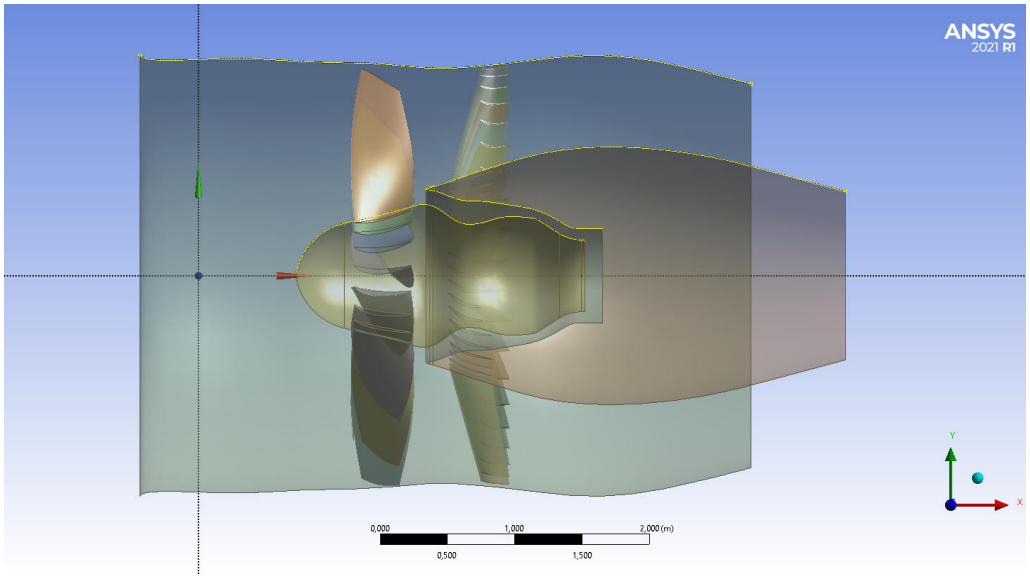

Figure 3.1: Section view of CAD geometry showing the low pressure section of the compression system.

In a Ph.D thesis by Marcus Lejon[20], an earlier iteration of this model was used, and will be used for comparison. Since this model, a number of design iterations have been carried out to the geometry. The most significant changes in the area of interest for this thesis are design changes to the nacelle. The differences in the models endwalls (hub and shroud lines) are shown in Figure 3.2. As can be seen, the earlier model doesn't include the spinner, which is a point of stagnation and will cause changes in the flow. Furthermore, the first portions of the hub and shroud lines uses a free-slip boundary condition, changing to no-slip at around axial coordinate 0.7. These changes causes small differences in the flow, but what is more important

is the difference in annulus area at the fan, as this is the location in the passage where we can expect the flow to choke first. The area of the current model is increased by approximately 2.5%, compared to the previous model. This means one should expect a slight increase in mass flow, using the same simulation set up. Also worth noting is that the current design of the engine is still a work in progress, and in no way the final design.

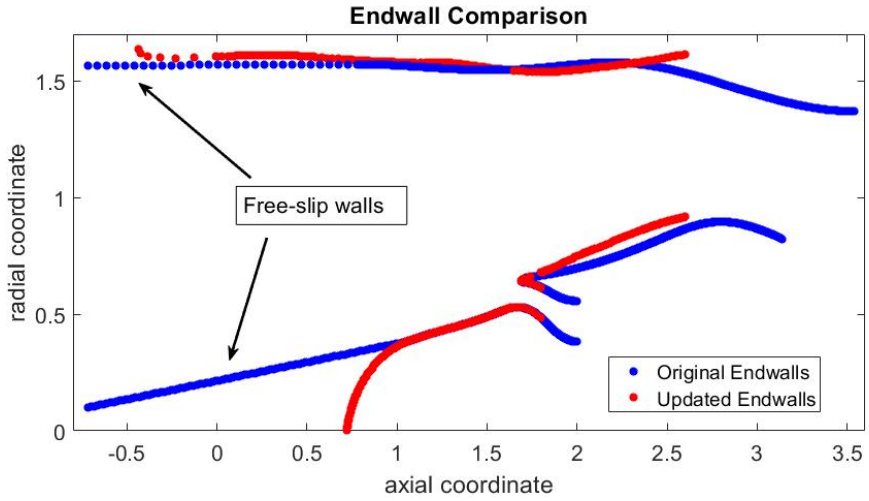

Figure 3.2: Difference in endwalls in original and current geometry.

3.1.1 Geometry export

The geometry is imported into the ANSYS software DesignModeler. This software is equipped with a tool to export turbomachinery components named Flowpath. This is done by defining the hub and shroud profile for the rotor and the stator. Then, by specifying the passage region, made up of hub, shroud, inlet, outlet, and respective blade, one can create layers on the blade, that are exported as points, together with the hub and shroud lines. This data can be directly imported into the meshing tool Turbogrid. The area in front of the rotor, consisting of the hub leading edge and shroud, as well as the area between the rotor and stator, consisting of splitter, hub, and shroud can be exported as hub and shroud lines. These are imported to the meshing tool Pointwise. The blade export feature is shown in figure 3.3.

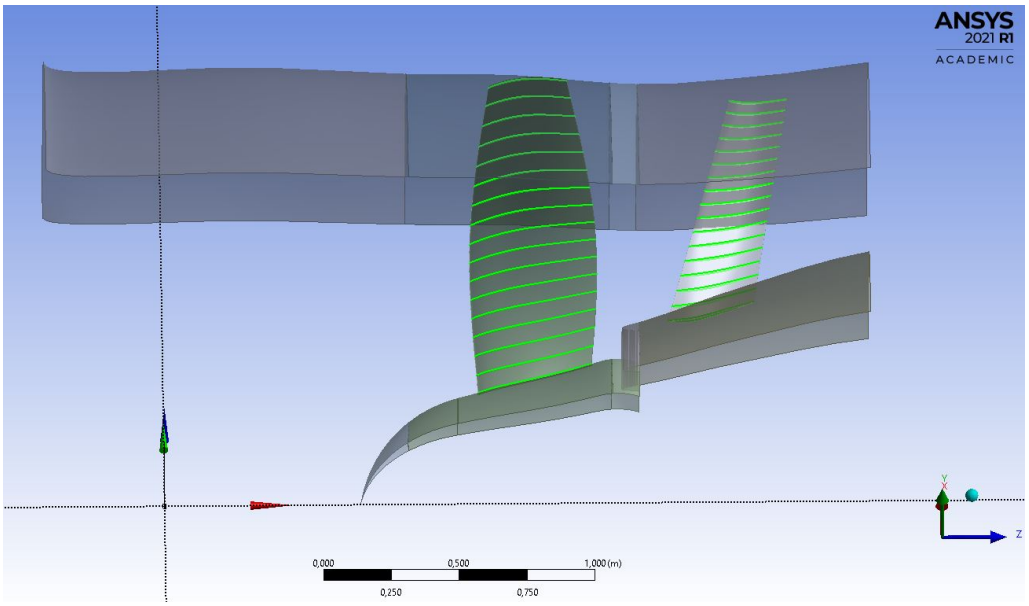

Figure 3.3: The blade layers exported as data points.

3.1.2 Computational domain and grid generation

The computational domain is divided in 4 sections, seen in Figure 3.4. These domains will be called inlet domain (number 1), the rotor passage (number 2), the splitter (number 3), and the stator passage (number 4).

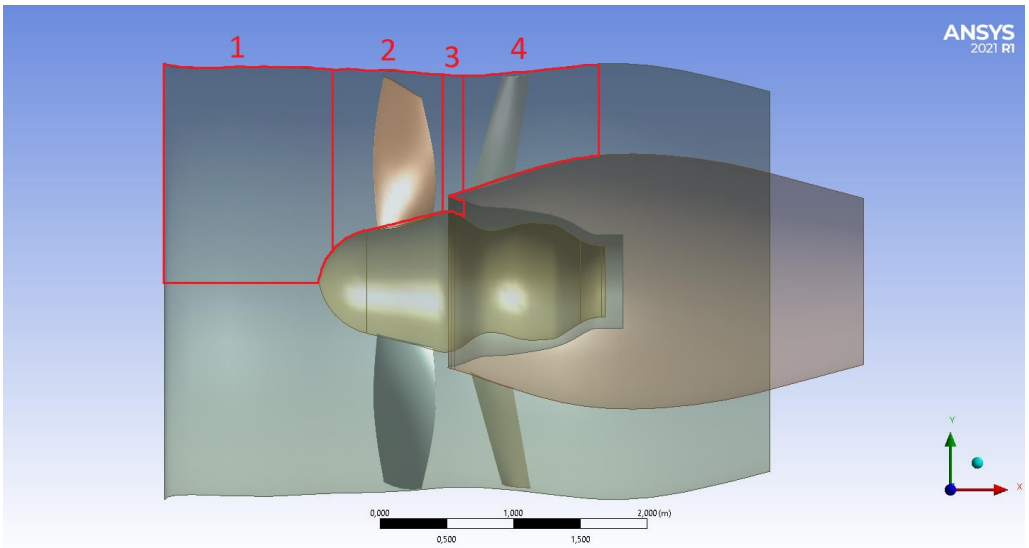

Figure 3.4: The modelled sections of the engine

For the fan blade and OGV blades the grid generator used is Turbogrid. Turbogrid is an automated grid generation tool within the ANSYS toolbox tailored for turbomachinery. Using this tool, it is simple to generate a high quality grid, and simple to include features such as tip clearance for the rotor. The boundary layers of the blades are in turn constructed using an o-grid and the rest of the passages are

constructed using an h-grid. As the passage of the fan is rotationally periodic, only one sector of the domain needs to be modelled. For the rotor and the stator, only a single blade passage is used in the computational model. In the rotor geometry, a tip clearence gap of 0.5% of span is specified, meaning that at the rotor tip, there is some clearance to allow for friction free rotation. The rotor passage and stator passage meshes from Turbogrid can be seen in Figures 3.5 and 3.6.

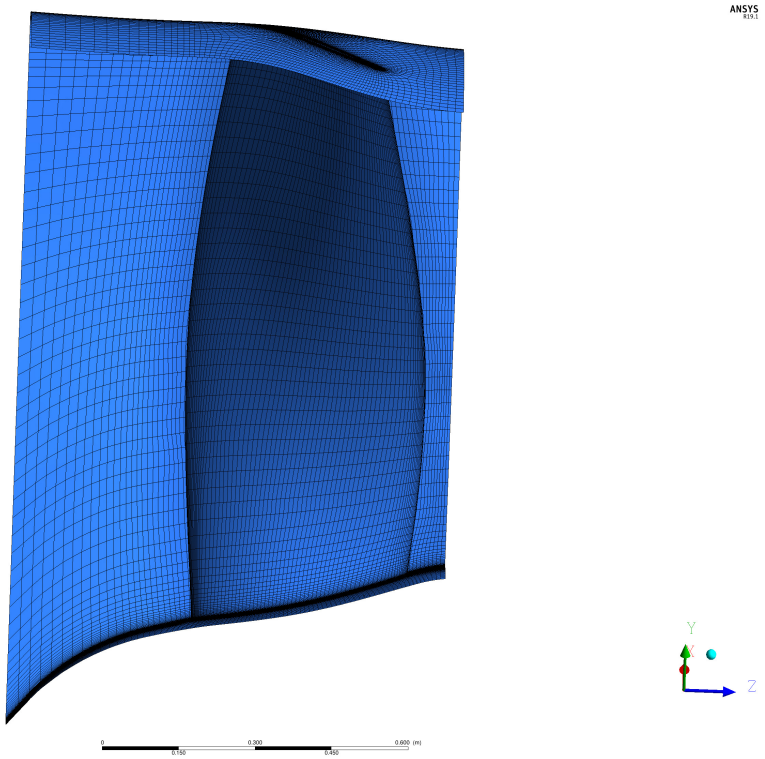

Figure 3.5: Mesh around the rotor blade as generated by Turbogrid.

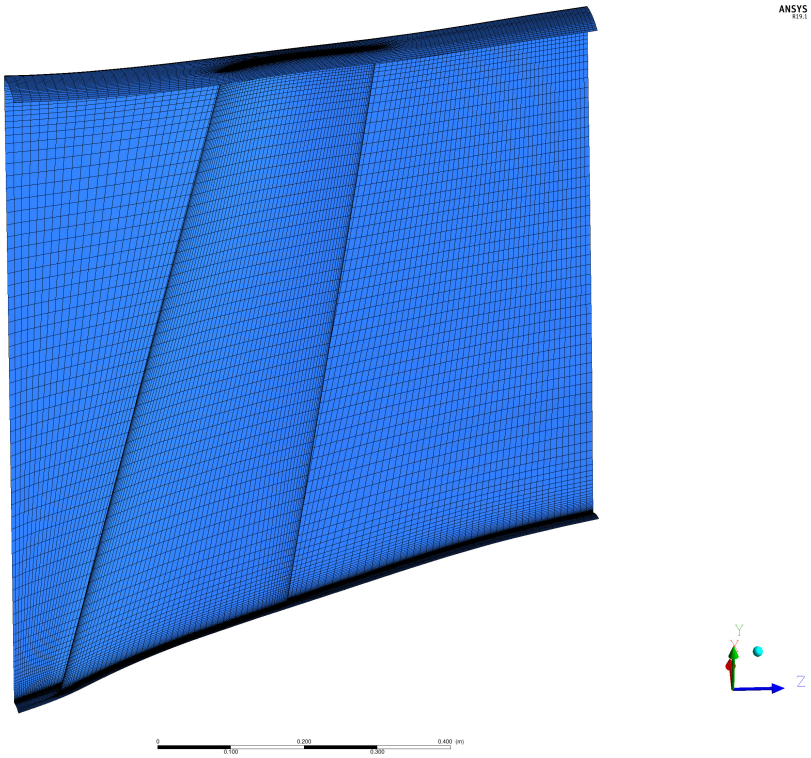

Figure 3.6: Mesh around the stator blade as generated by Turbogrid.

To generate the mesh for the inlet domain and splitter the meshing software Pointwise is used. The geometry hub, shroud and splitter lines are imported as 2D curves into Pointwise. On these, a 2D structured H-grid is generated by specifying element counts on each curve. On the splitter surface and on the inlet domain hub, an O-grid is used to for the boundary layer. These 2D structured grids are then extruded rotationally around the z axis to get a section of the annulus. As the hub and shroud lines are rotationally symmetric, only a portion of the domain needs to be modelled. The complete annulus is then taken into account by applying a rotational periodic boundary condition in CFX.

Depending on the chosen turbulence model, the grid close to the walls have different requirements that must be fulfilled. In the k - ω SST model the boundary layer should be resolved, meaning that a cell height close to the walls that ensures a $y^+ < 1$ is required. Using an expected Reynolds number of approximately $1.5 \cdot 10^6$, the first cell of the boundary layer is around 1.7 μm thick. In Figures 3.7 and 3.8 the meshes for the splitter and inlet domain can be seen.

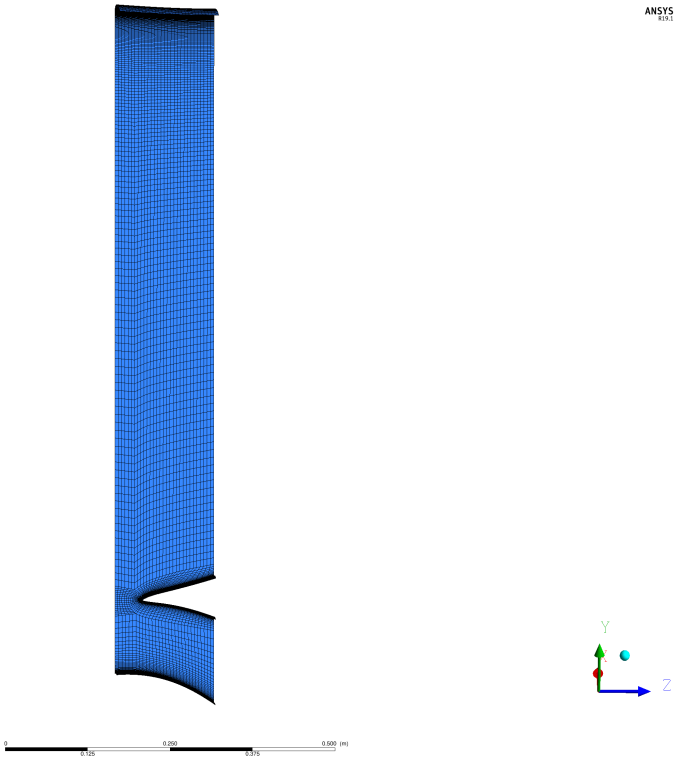

Figure 3.7: The mesh in the splitter.

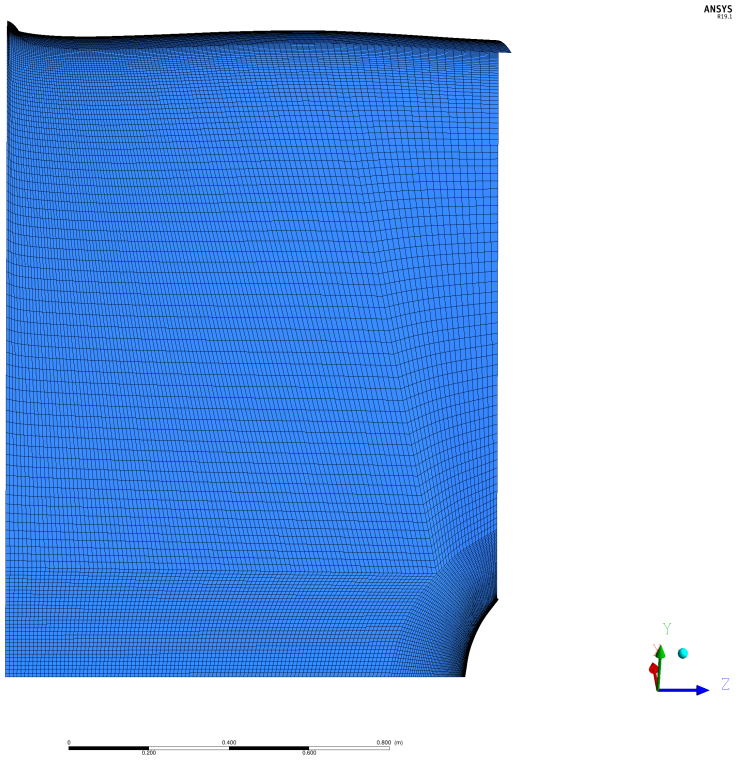

Figure 3.8: The mesh in the Inlet domain.

3.1.3 Boundary conditions

In order to achieve a proper solution, proper boundary conditions are needed. These will not only affect the final solution, but also how it converges and how stable it is. As the current case involves a large domain with transsonic flow, stability is very important, and boundary condition choices are based around this. The case is run in steady state mode, and a single blade passage is used, using periodic boundary conditions to account for the entire annulus.

The inlet condition is specified as constant total pressure and total temperature, and medium intensity (5 %) turbulence. The two outlets are specified by average static pressure with a pressure profile blend of 0.05. The hub, shroud, and rotor blade are set to be adiabatic no-slip walls, while the stator blade are set as a no-slip wall with a specified temperature, since it will be acting as a heat exchanger in our studies. The domain is divided into multiple subdomains. The interface between these is mixing plane. Mixing planes are frequently used in steady state turbomachinery simulations featuring multiple components of different blade counts. This circumferentially averages the flow variables in the rotational direction, allowing connection of domains of different sizes. In addition to this, no periodic effects such as wakes created by the rotating blade will be observed. The rotor subdomain is set to rotate around the z axis, with the exception of the shroud, which is specified to counter rotation. At the tip clearance in the rotor, a general connection is specified between the suction and pressure side, the tip clearance is specified to be 0.5% of the span. The domain is shown in Figure 3.9.

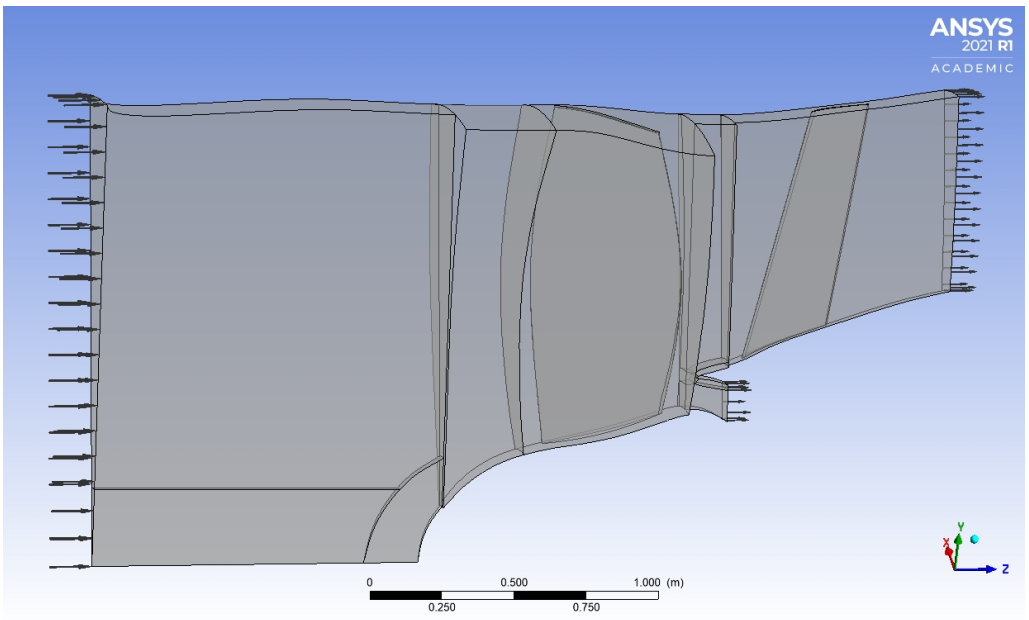

Figure 3.9: Computational domain of the rotor and OGV shown in CFX pre.

3.1.4 Low aspect ratio OGV geometry

In addition to the geometry presented above, another set of OGV blades are available for the fan. This set of blades are based on the original blade, but extended in the axial and rotational direction to create substantially larger blades, while conserving blade solidity. Because of their size, only 9 blades are used in the annulus, as compared to the orginial 43. A side by side comparison of the blades are given in Figure 3.10, where the front blade shows the original OGV and the back blade is the low aspect ratio OGV.

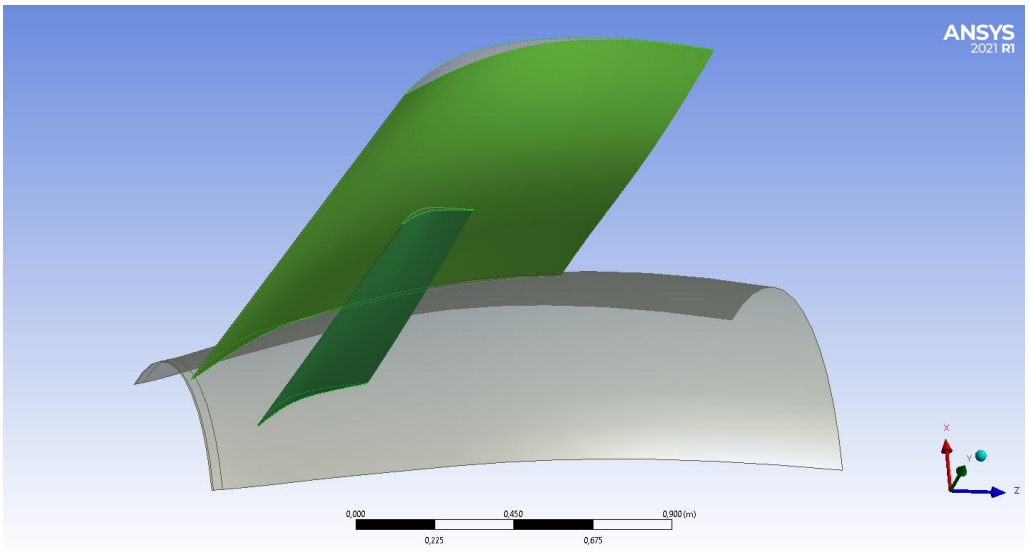

Figure 3.10: Side by side comparison of the two OGV geometries.

As these blades are thicker and longer than the original blades, they might be a good candidate for the cooling system as this means one can potentially fit more cooling pipes inside. As the flow through the fan can be established by the earlier simulations, only the OGV flow needs to be modelled in this case. This is implemented by extracting data from a plane in the full fan simulation. The data exported are total pressure, total temperature, and velocity direction. This can then be used as an inlet boundary condition for only the OGV.

As this is only done as a heat transfer comparison to the original OGV blades, no attention will be paid to the whole fan performance using these blades. As the simulated cross section is much larger, 1/9 instead of around 1/43 of the annulus, the inlet boundary condition taken from the previous simulations have to be extended to cover the entire stator inlet. This is done by extracting the plane data, containing coordinates and the boundary conditions mentioned, and importing into MATLAB. Because of the use of mixing planes and steady state simulation, the domain and variables are completely rotational symmetric about the axis of rotation (the z axis), the data from the plane can be extended rotationally by multiplying with a rotational matrix as

$$R_z = \begin{bmatrix} cos(\theta) & -sin(\theta) & 0 \\ sin(\theta) & cos(\theta) & 0 \\ 0 & 0 & 1 \end{bmatrix} \tag{3.1}$$

Where θ is the desired rotation, in this case about 8° to match the size of the domain. Applying this rotation to the coordinates and the velocity vector and merging the geometries will increase the width to about 16°, and the same pattern can be repeated to recreate the full annulus if desired.

3.2 Data Processing

The primary objective of the CFD simulations is to obtain the heat transfer coefficient on the OGV. As flow properties such as temperature and velocity change along the blade, one can expect the heat flux and therefore the heat transfer coefficient to also vary along the blade. ANSYS CFX calculates heat transfer coefficient as

$$h = \frac{Q}{T_w - T_{ref}} \tag{3.2}$$

where T_w is the static temperature of the cell closest to the wall and T_{ref} is the reference static temperature, which is set to be the second element from the wall. In this case, this formulation is not very useful, as the near wall temperature differs over the blade. The reference temperature is also used as an input in the modeling on system level, and it is more convenient to have a constant reference temperature. Because of this, the bulk temperature, which is the average flow in the passage, is used as reference temperature. This is achieved by either manually specify T_{ref} in the simulation set up using an expert parameter, or to create a variable in post processing. The latter of these was done, setting up a variable in CFX post as

$$\textit{Heat Flux}/(\textit{Temperature} - \textbf{massFlowAve}(\textit{Temperature})@\textbf{Stator Inlet}) \tag{3.3}$$

This will, instead of using near wall temperature, use a mass flow averaged temperature at the OGV domain inlet to calculate the heat transfer coefficient. To use this data in junction with the data for the internal cooling system, the heat transfer coefficient (HTC) is exported into MATLAB, as a matrix containing the coordinates and HTC for each cell along the blade. To simplify the 3D heat transfer problem, the heat transfer coefficient is radially averaged weighed by element length such as

$$h_{avg} = \frac{\Sigma L_e h_e}{\Sigma L_e} \tag{3.4}$$

Where h_e is element heat transfer coefficient and L_e is element length. This means that for a given % of span, only a single HTC exists. With an averaged heat transfer coefficient, the problem is simplified to a 2 dimensional problem, which is easier to solve.

3.3 Flat plate

The flat plate study was performed to validate the heat transfer coefficient obtained using the CFD tool, CFX. The flat plate case was studied in two different instances. One case with similar boundary condition as that of the OGV operated at cruise. Similarly, the other case at idle condition. The heat transfer coefficient calculated in CFX was validated by comparison with correlations from literature. The domain used to represent flat plate is quite simple. It consist of a chord length of 0.25 m and is represented by a no-slip wall boundary condition. Also, a part of the domain is a free-slip wall with a length of 0.05 m, located before the leading edge. Inlet and outlet boundary conditions are specified on the left and right boundaries of the domain respectively. Symmetry boundary condition is used on the top and sides of the domain. The flat plate domain is as shown in Figure(3.11).

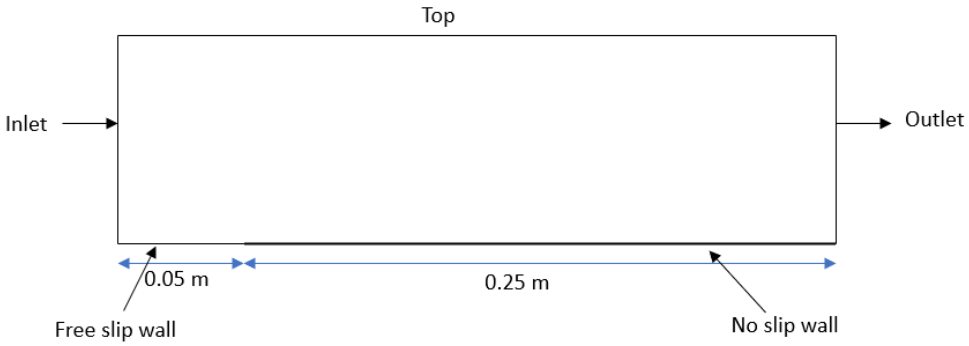

Figure 3.11: Flat plate geometry.

The exact boundary conditions used for the cruise and the idle case are given in Appendix A.1. These cases were solved using the k - ω SST turbulence model along with the γ - θ turbulence transition model. The correlations used are shown in equation (3.5) for laminar flow and equation (3.6) for turbulent flow[14].

$$Nu_x = 0.332 Re^{1/2} Pr^{1/3} \left(\frac{T_{surf}}{T_\infty}\right)^{-n} \tag{3.5}$$

$$Nu_x = 0.0296 Re^{4/5} Pr^{1/3} \left(\frac{T_{surf}}{T_\infty}\right)^{-n} \tag{3.6}$$

where $\left(\frac{T_{surf}}{T_\infty}\right)^{-n}$ is the correction factor for property variation due to change in static temperature across the boundary and the exponent n is between 0.25 to 0.45[14].

3.4 Wall resistance

To account for the wall resistance factor an empirical correlation was derived using steady state heat transfer simulations. This correlation uses two variables to account for variations in geometry. These are the wall thickness and the distance between the pipes. Both of these are defined in relation to pipe diameter. The geometry setup

is shown in Figure 3.12, and the simulations are carried out in 2D. The symmetry boundary conditions are indicated by dotted lines in the figure, while the full drawn lines indicate walls. The heat transfer is measured between the upper wall which represents the outside of the OGV, and the two lower walls, which represent the inner pipe surfaces.

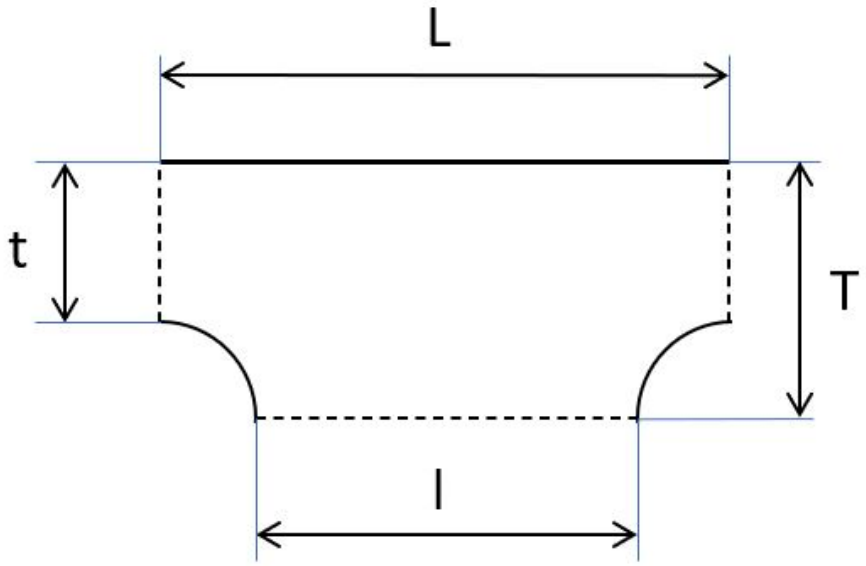

Figure 3.12: Geometry for wall resistance simulations.

Using the parametrization tool in the ANSYS workbench, multiple simulations can be run in succession. By doing this, all possible geometry permutations in the span of the two parameters can be evaluated. The range assumed for each geometrical parameter is

$$1.5 < \frac{T}{t}, \frac{L}{l} < 6 \tag{3.7}$$

where T and t are maximum and minimum thickness, and L and l are maximum and minimum length, shown in Figure 3.12. The wall resistance is given by

$$R_{wall} = \frac{T_{pipe} - T_{wall}}{q} \tag{3.8}$$

Where T_{pipe} is set to 393 K, T_{wall} is set to 293 K, and Q is the results from the simulations. This data is then imported to matlab where curve fitting toolbox is used to establish a correlation. To see the effect the material properties of the OGV on the heat transfer, two different materials are simulated. These two are the titanium alloy Ti6Al4V and the aluminium alloy 2219. The properties of these two are given in Table 3.1. These are chosen quite arbitrarily, based on choosing one alloy with good heat transfer properties and one with bad. Also worth keeping in mind is that the increase in heat transfer comes at a cost of reduced mechanical strength.

Property	Ti6Al4V	Aluminium 2219	Unit
Specific heat capacity	560	864	[J/kg K]
Thermal conductivity	7.2	143	[W/m K]
Density	4470	2840	[kg/m^3]
Young's modulus	125	73.8	[GPa]

Table 3.1: Material propeties of the two used alloys.

3.5 Piping

The internal cooling system is made up of pipes, i.e, one pipe coming from the generator, that is subdivided into a number of pipes and each pipe passing through one blade individually, and connecting back to the core. Different pipe positions in the blade will give different outcome, as variables such as pipe thickness as pipe length will vary through the blade. Some simplifications are made to the pipe system to make it more manageable. For starters, no simulations of this will be done, and only theoretical and numerics will be used. Furthermore, the OGV blades are slightly curved around the axis of rotation, this will not be taken into account, as the blades will be modelled to be straight. Pipes are also assumed to be placed at a constant span location on the OGV. The blades are also assumed to have a strict linear tapper from hub to shroud, and all calculations are based on hub, shroud, or mean values. A proposed pipe setup is shown in Figure 3.13, note that pipe thickness is not shown, only locations of pipe. Number 1 in the figure indicates direction of the incoming air flow, 2 and 3 are the inlet and outlet to the piping system, respectively. Also shown are two of the design variables. Number 4 shows the distance between leading edge and first pipe, henceforth called first pipe location and given in percentage of span wise length. Number 5 shows the distance between pipes, as taken at the hub, given in centimeters.

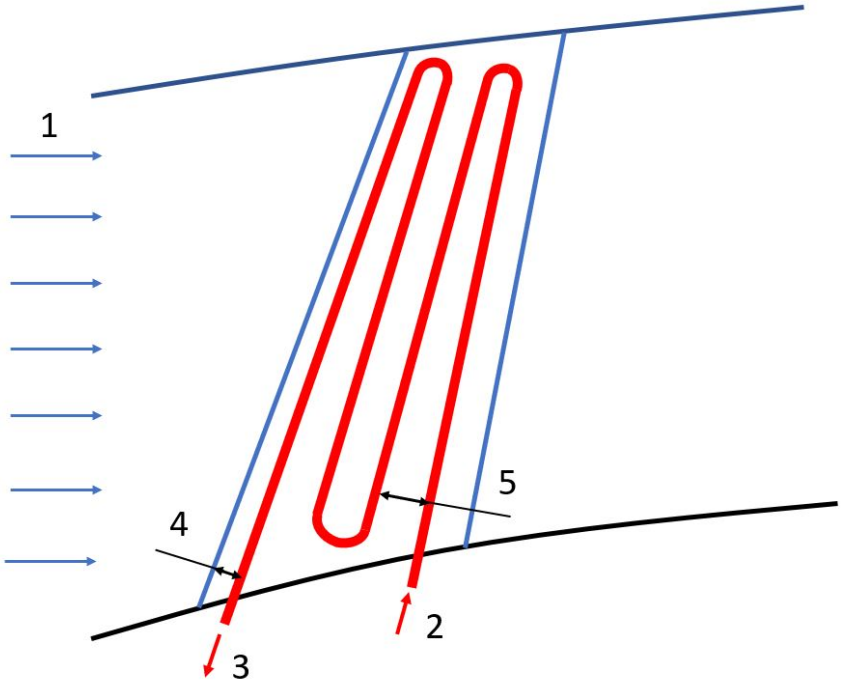

Figure 3.13: A proposed pipe configuration inside the OGV.

The flow in the pipe is based on a provided value for total volume flow for all OGVs of

$$Q = 0.0012 \frac{m^3}{s} \tag{3.9}$$

meaning that each OGV pipe system will have a flow of

$$Q_n = \frac{Q}{n} \tag{3.10}$$

where n is the number of OGV used for cooling. The inlet and mean temperature of the coolant as 393.15K and 368.15K respectively was also provided. Using volume flow and pipe diameter, velocity can be calculated in the pipes as

$$v = \frac{Q_n}{A} = 4\frac{Q_n}{D^2\pi} \tag{3.11}$$

Reynolds and Prandtl numbers were calculated using equations (2.51) and (2.52) respectively, both of these will depend on the choice of coolant inside the pipes, and different fluids have different viscosity and heat transfer properties. Based on this, the Nusselt number can be calculated using the correlations. For laminar flow, fully developed conditions, the Nusselt number is approximated to be a constant, independent of Re, Pr and axial location[11].

$$Nu = 3.66 \tag{3.12}$$

For turbulent flow, correlation provided by Gnielinski[10] was used,

$$Nu = \frac{(f/8)(Re - 1000)Pr}{1 + 12.7(f/8)^{1/2}(Pr^{2/3} - 1)} \tag{3.13}$$

where f is the Darcy friction factor[10],

$$f = \left(1.8 \log \frac{Re}{6.9}\right)^{-2} \tag{3.14}$$

The Gnielinski correlation is valid for $0.5 \leq Pr \leq 2000$ and $3000 \leq Re \leq 5 \times 10^6$ [10].
Now the internal heat transfer coefficient can be obtained as

$$h_i = \frac{k \cdot Nu}{D} \tag{3.15}$$

where k is the thermal conductivity of the coolant. Furthermore, the total wetted area for the pipes can be obtained as

$$A_{wetted} = \sum_{i=1}^{n} \pi D_i L_i \tag{3.16}$$

where D_i and L_i is the diameter and length of pipe i.
The factors that contribute to pressure loss in the pipes are frictional losses, losses due to change in diameter of pipes (i.e., sudden expansion and contraction), and losses due to pipe bends. The losses are only measured in the OGV, meaning losses that occur to and from the generator are ignored. The frictional losses were calculated using equation (3.17) in a single pipe and is summed up over the number of pipes.

$$\Delta P_f = f \frac{L_i}{D_i} \frac{\rho_i v_i^2}{2} \tag{3.17}$$

where f is friction factor obtained using equation (3.14), L_i and D_i are the length and diameter of the pipe i and v_i is the velocity in the corresponding pipe.
The losses due to change in diameter and bend in pipes are usually expressed in terms of velocity head and a coefficient, as shown by the equation

$$h_m = K \frac{v^2}{2g} \tag{3.18}$$

where K is a dimensionless parameter called head loss coefficient.
For sudden expansion, the coefficient is obtained from the equation,

$$K_{SE} = \left(1 - \frac{d^2}{D^2}\right)^2 \tag{3.19}$$

where d and D are the diameters of the pipe before and after expansion respectively, and K_{SE} is the loss coefficient due to sudden expansion[12].

The coefficient for sudden contraction is obtained from the following empirical formula,

$$K_{SC} = 0.42 \left(1 - \frac{d^2}{D^2}\right) \tag{3.20}$$

where D and d are the diameters of the pipe before and after contraction respectively, and K_{SC} is the loss coefficient due to sudden contraction.

The loss at a bend is because on the curved wall the flow separates and also a swirling secondary flow occurs due to the centripetal acceleration[12]. The head loss coefficient for 180° bend in pipes was obtained from the plot in the textbook of fluid mechanics[12]. The data points of the curve was extracted and plotted in MATLAB and the curve fitting toolbox was used to get the curve-fit formula,

$$\begin{aligned} K_b = a_0 &+ a_1 * cos(R*w) + b_1 * sin(R*w) \\ &+ a_2 * cos(2*R*w) + b_2 * sin(2*R*w) + a_3 * cos(3*R*w) \\ &+ b_3 * sin(3*R*w) + a_4 * cos(4*R*w) + b_4 * sin(4*R*w) \end{aligned} \tag{3.21}$$

where K_b is the loss coefficient due to bend, R is the radius of bend, a_0 to a_4, b_1 to b_4 and w are constants determined by the curve fitting tool. The constant values are as follows,

$$\begin{bmatrix} a_0 \\ a_1 \\ b_1 \\ a_2 \\ b_2 \\ a_3 \\ b_3 \\ a_4 \\ b_4 \\ w \end{bmatrix} = \begin{bmatrix} 11.86 \\ 2.584 \\ -18.82 \\ -10.58 \\ -3.486 \\ -1.998 \\ 3.703 \\ 0.6247 \\ 0.5041 \\ 0.1895 \end{bmatrix} \tag{3.22}$$

After obtaining all the coefficients the head losses were calculated using equation (3.18) and finally the pressure losses were calculated using the Bernoulli's equation (2.55). Finally, the pumping power was calculated using equation,

$$W_{pump} = \Delta p Q / \eta_p \tag{3.23}$$

Where Δp is the pressure drop, Q is the volumetric flow rate, and η_p is the pump efficiency, this is set to unity.

3.5.1 Coolant

There are wide range of cooling fluids available currently. Selection of a suitable coolant can be quite complicated as it involves taking into account several factors like the composition, physical properties, thermal stability, performance, compatibility and maintenance. However, the range of options were narrowed down based on the operating range requirement, compatibility with electric devices and a coolant was decided based on an optimum balance between heat transfer performance and pressure loss. Physical properties of the fluid that affect the heat transfer performance like density, viscosity, thermal conductivity and specific heat were obtained

from a software which contains the database of the fluids called CoolProp. The fluids that were selected were Dowtherm J, Paratherm LR, Therminol D12, Syltherm XLT and ethylene glycol/water mixture at concentration 50, 60, 70, 80, 90 and 100%. Table 3.2. shows the temperature range of the coolants.

Coolants	Temperature range (°C)
Dowtherm J	-80 to 315
Paratherm LR	-85 to 230
Therminol D12	-94 to 230
Syltherm XLT	-100 to 260
50% Ethylene Glycol	-50 to 120
60% Ethylene Glycol	-50 to 120
70% Ethylene Glycol	-50 to 120
80% Ethylene Glycol	-50 to 120
90% Ethylene Glycol	-50 to 120
100% Ethylene Glycol	-50 to 120

Table 3.2: Temperature range of different coolants

3.6 Heat exchanger performance

There are two methods for estimating the performance of heat exchangers, the log-mean temperature difference(LMTD) or the effectiveness-NTU method. The LMTD method is usually employed to calculate the surface area of heat exchanger, when the fluid inlet temperatures and outlet temperatures are known or can easily be determined. If only inlet temperatures of the fluid are available, then the LMTD approach would be complex as it would require cumbersome iterative process to obtain the solution[11]. In this project, the focus is to integrate the heat exchanger into the fan OGV and determine if the heat load requirements are met. The surface area of the OGV is available and the inlet temperature of the fluids are known, hence it is a preferable approach to use the effectiveness-NTU method.

3.6.1 The effectiveness-NTU method

Effectiveness is the ratio of actual heat transfer to the maximum possible heat transfer.

$$\epsilon = \frac{q}{q_{max}} \tag{3.24}$$

First, the maximum possible heat transfer was calculated using,

$$q_{max} = C_{min}(T_{h,i} - T_{c,i}) \tag{3.25}$$

where $T_{h,i}$ and $T_{h,c}$ are the inlet temperatures of hot and cold fluid respectively, used to obtain the maximum temperature difference in the heat exchanger. C_{min} is equal to heat capacity of cold fluid(C_c) or hot fluid (C_h), whichever is smaller. This is because the fluid with smaller heat capacity will be the one to experience maximum temperature change earliest, which would mark the cease of heat transfer. The heat

capacity were obtained using equation (3.26) and equation (3.27) for hot and cold fluid respectively.

$$C_h = \dot{m}_h c_{p_h} \tag{3.26}$$

$$C_c = \dot{m}_c c_{p_c} \tag{3.27}$$

where $\dot{m}_h$ and c_{p_h} are mass flow and specific heat capacity of hot fluid respectively, and $\dot{m}_c$ and c_{p_c} are mass flow and specific heat capacity of cold fluid respectively.

The number of transfer units (NTU) is a non-dimensional expression of the thermal size of the exchanger[13] and is defined as,

$$NTU = \frac{UA}{C_{min}} \tag{3.28}$$

The product UA was determined using the overall heat transfer coefficient equation(2.53) and knowing this, the NTU was calculated. It is assumed that the total NTU is equally distributed between each pass and also both the fluids are unmixed. The effectiveness per pass for cross-flow heat exchanger was calculated using the correlation,

$$\epsilon_p = 1 - exp\left[\frac{1}{C_r}\left(\frac{NTU}{n}\right)^{0.22}\{exp[-C_r\left(\frac{NTU}{n}\right)^{0.78}] - 1\}\right] \tag{3.29}$$

where ϵ_p is the effectiveness of each pass, n is the number of identical passes and $C_r = \frac{C_{min}}{C_{max}}$ is the heat capacity ratio.
Then, the total effectiveness of the heat exchanger was obtained using,

$$\epsilon = \frac{\left(\frac{1-\epsilon_p C_r}{1-\epsilon_p}\right)^n - 1}{\left(\frac{1-\epsilon_p C_r}{1-\epsilon_p}\right)^n - C_r} \tag{3.30}$$

The total heat rejected from the hot fluid, in this case coolant, to the cold fluid air, which is dependent on the effectiveness of the heat exchanger, was finally calculated using equation(3.24).

3.6.2 Optimization

In the problem at hand, no optimal solution exists that minimizes both pressure drop and maximizes heat transfer. Instead, a multi-objective optimization problem have to be solved. The problem looks like

$$\begin{bmatrix} -q \\ \Delta P \end{bmatrix} = \begin{bmatrix} f_1((x, N, \delta, c) \\ f_2((x, N, \delta, c) \end{bmatrix} = \begin{bmatrix} f_1(\mathbf{x}) \\ f_2(\mathbf{x}) \end{bmatrix} \tag{3.31}$$

Where x is the location of the first pipe, N is the number of pipe passes, and δ is a constant set diameter between pipes, and c is the coolant used. The reason that the heat transfer is taken as a negative is that the optimization solves the problem

$$\min(f_1(\mathbf{x}), f_2(\mathbf{x})) : \mathbf{x} \in \mathbf{X} \tag{3.32}$$

where $\mathbf{X}$ is a set of all feasible decisions, or inputs. To do this, a brute force genetic algorithm is applied. This algorithm will, based on a set of constraints on the input variables, generate a first population of possible inputs. These solutions will be evaluated with the objective to maximize heat transfer and minimize pressure drop. The best suited individuals are selected for the next generation, along with cross-overs and mutations of individuals. This process will go on until a convergence criterion is met or the maximum number of generation criterion is met. For this, the MATLAB tool GAmultiobj is used. However, since this tool uses float point values as inputs, the population, cross-over, and mutation algorithms have to be altered, as pipe number have to be an integer. This is simply done by using the existing functions and adding a section that will randomly round up or down to an integer for the integer variable. A solution $\mathbf{x_1} = (x_1, N_1, \delta_1, c_1)$ is called Pareto optimal if it cannot be improved in one variable without impairing another. This is described by

$$f_i(\mathbf{x_1}) \leq f_i(\mathbf{x_2}) \; \forall \; i \in 1, 2 \tag{3.33}$$

$$f_j(\mathbf{x_1}) < f_j(\mathbf{x_2}) \; \exists \; j \in 1, 2 \tag{3.34}$$

where $\mathbf{x_1}$ is Pareto dominant to $\mathbf{x_2}$. The output from the code is a range of solutions that all are Pareto optimal, forming a Pareto front.

4

Results

4.1 Simulations

In this chapter, the results of CFD RANS simulations in cruise and ground idle will be shown, after validating the mesh by doing a mesh independence study. The simulations are carried out in ANSYS CFX using a $k-\omega$ SST model with the $\gamma-\theta$ turbulence transition model. First, a flat plate simulation is shown.

4.1.1 Flat plate example

In this section, the results from the simulations are compared with the correlations. Figure 4.1, shows the plot of heat transfer coefficient over the length of the flat plate for idle condition and Figure 4.2, shows the plot for the cruise case.

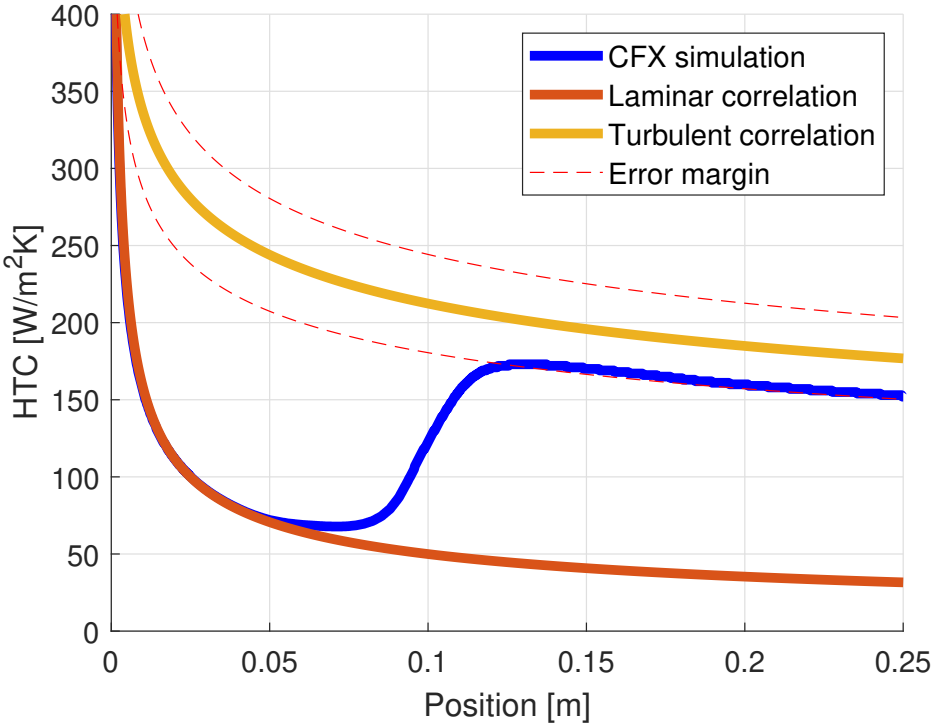

Figure 4.1: Heat transfer coefficient comparison for idle case.

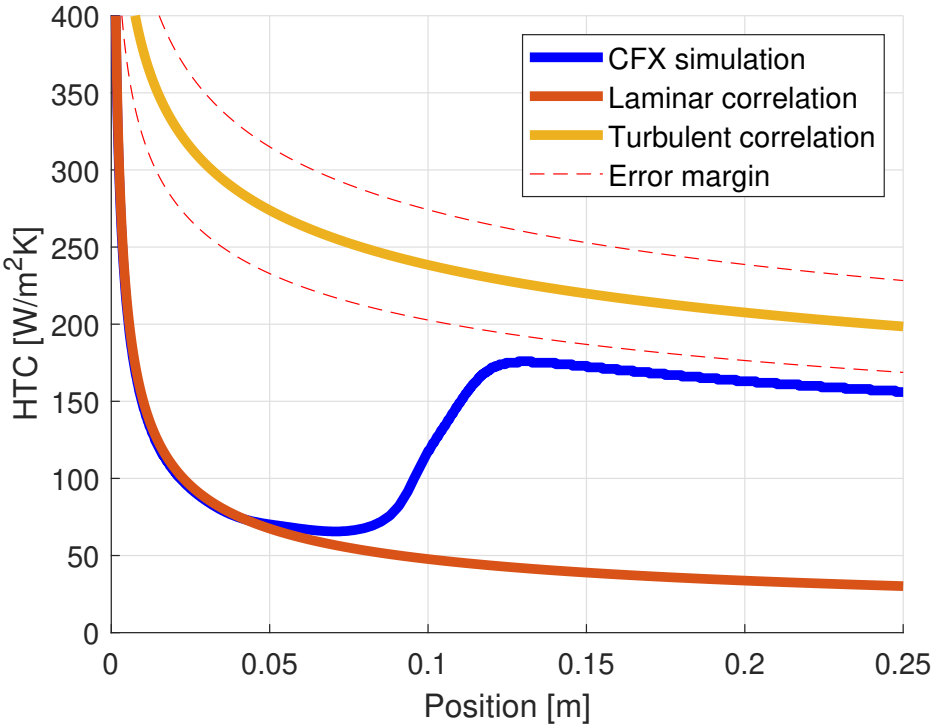

Figure 4.2: Heat transfer coefficient comparison for cruise case.

It can be observed that CFD result and the laminar correlations are in quite a good agreement with each other for both the cruise and idle case. However, for the turbulent region, offset is observed. The HTC curve obtained by simulation is below the curve calculated from turbulent correlation. An error margin of 15% is drawn around the results obtained from turbulent correlation[14]. It can be seen that for the idle case, the simulation results are within the error margin but for the cruise case it is outside the error margin. It was noticed that, for high Mach numbers, the deviation of the CFX results from turbulent correlation increases. Since, the goal was to achieve a minimum heat rejection of 20 kW, this under estimation of CFX results was decided to be acceptable.

4.1.2 Cases

To establish the performance of the heat exchanger, multiple cases needs to be studied, to account for the different operating conditions caused by the the external conditions. The two studied cases are cruise and ground idle. The exact boundary conditions used are given in Appendix A.2. Cruise is defined as the operating condition when the airplane is flying at constant velocity and at a constant altitude, while in ground idle, the airplane is standing still on the ground with engines running at a low rotational speed.

4.1.3 Mesh independence study

In order to investigate the impact of mesh resolution on the solution, a mesh independence study is carried out. This study is done by altering the resolution of a mesh, from rough to very fine, and study how the results are changing from mesh to mesh. If the solution is not changing, it is said to be mesh independent. This is of course very important as a validation tool because flow phenomena occurring is then more likely caused by the geometry than the computational domain. It is also an important tool in order to save computational resources. If the solution is close to invariant with mesh refinement, very little is achieved by refining the mesh except increasing the computational cost. The base mesh was generated with y^+ below 1 to ensure that wall functions would not activate. The cell counts in the different regions is shown in Table 4.1.

	Inlet	Splitter	Rotor	Stator	Total
Very Coarse	100000	77000	881000	653000	1711000
Coarse	156000	123000	1366000	963000	2607000
Medium	241000	171000	2029000	1343000	3785000
Fine	430000	321000	2291000	1718000	4760000
Very Fine	552000	515000	2940000	2414000	6421000
Extremely Fine	737000	629000	5694000	3185000	10245000

Table 4.1: Mesh independence study cell counts.

The parameters used in the mesh independence study are the mass flow, the bypass ratio, and the fan pressure ratio.These are all measured as the simulation has reached convergence. By comparing the parameters in terms of percentage of solution computed in the extremely fine grid, one can plot how the parameters of interest vary as the grid resolution is increased. This is shown in Figure 4.3. Here, it is deemed that the fine mesh is sufficiently accurate, and will be used for all further results using this geometry. For the case with the low aspect ratio OGV, a mesh of the same element size as the regular OGV mesh is created.

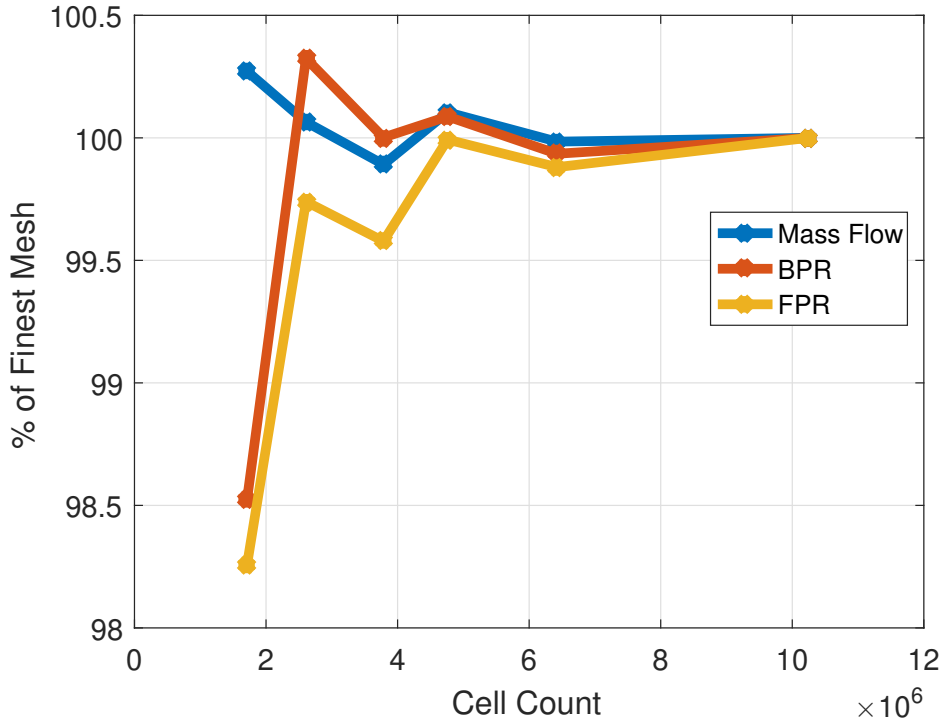

Figure 4.3: Mesh independence study as percentage of final solution

4.1.4 Cruise

For cruise, the fan performance map is shown alongside the data based on the earlier version of the geometry in Figure 4.4. The surge margin (equation 2.5), based on the simulation data, is around 16%. Comparing to the previous data, the surge margin is around 18%, seeing as the surge mass flow is very similar, this can be attributed to the slightly higher fan pressure ratio. The higher pressure ratio is most likely due to the fact that it is run at a higher rotational speed. A decrease in rotational speed of 3.7% is used due to the different endwalls causing the mass flow to increase. To keep the mass flow constant, the rotational speed have to be lowered to shift the speedline back to the design point. This affects the fan pressure ratio.

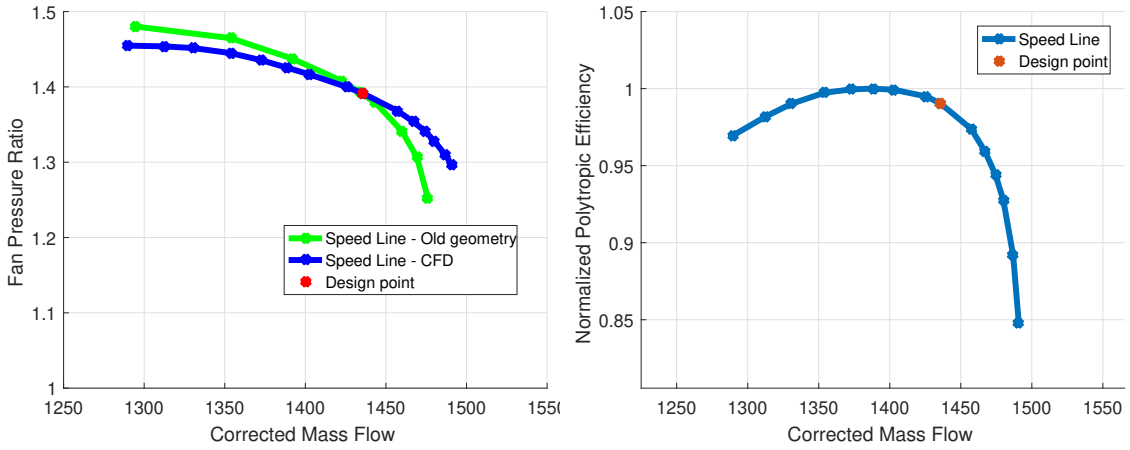

(a) Fan pressure ratio **(b)** Polytropic efficiency

Figure 4.4: Mapping of the cruise case

4.1.4.1 Heat transfer coefficient

In Figure 4.5 and Figure 4.6, the heat transfer coefficient on the suction and pressure side of the OGV blade can be seen. On the suction side, one can clearly see the transition from laminar to turbulent. Close after the leading edge the heat transfer coefficient is low, with a sudden increase moving downstream, a typical characteristic of transition. On the pressure side, the bottom half of the OGV the transition is seen close to the leading edge, meaning a larger portion of the area is turbulent. The average heat transfer coefficient on the entire blade is 165.5 W/m^{2}K.

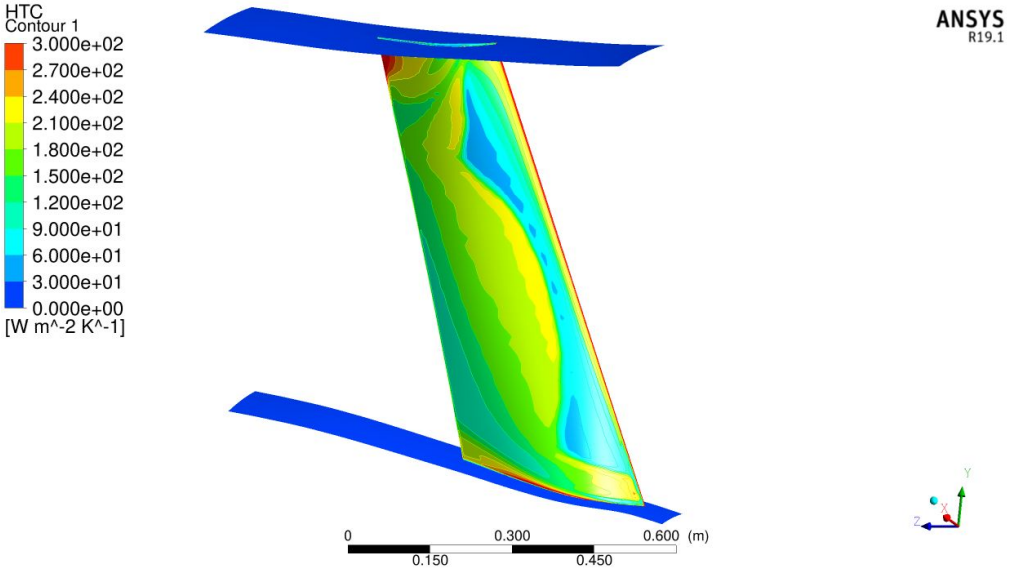

Figure 4.5: Heat transfer coefficient on the suction side of the OGV blade in cruise.

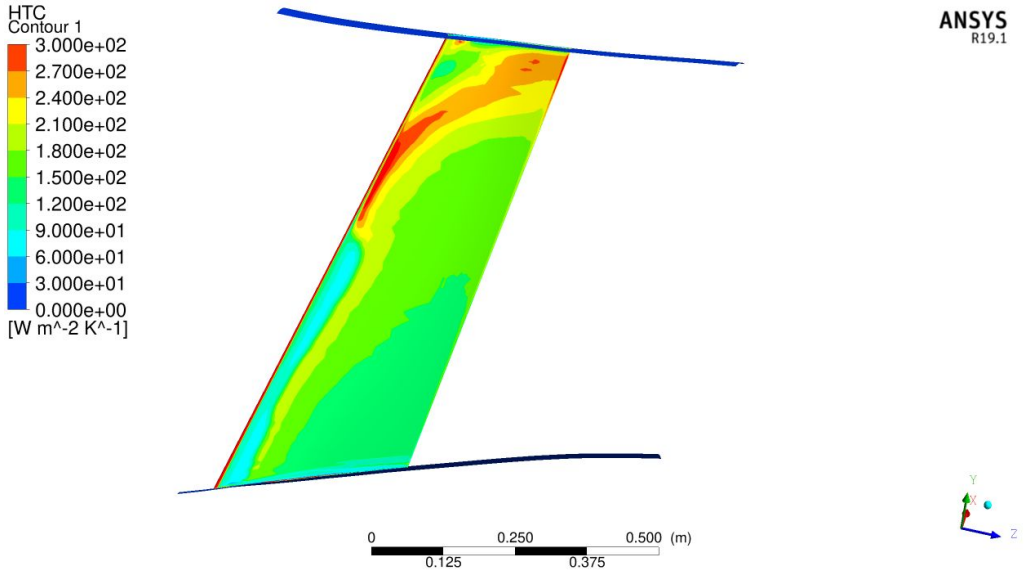

Figure 4.6: Heat transfer coefficient on the pressure side of the OGV blade in cruise.

In Figure 4.7 the heat transfer coefficient distribution is shown along three heights, one close to the hub (5%), one close to the shroud (95%) and one in the middle (50%).

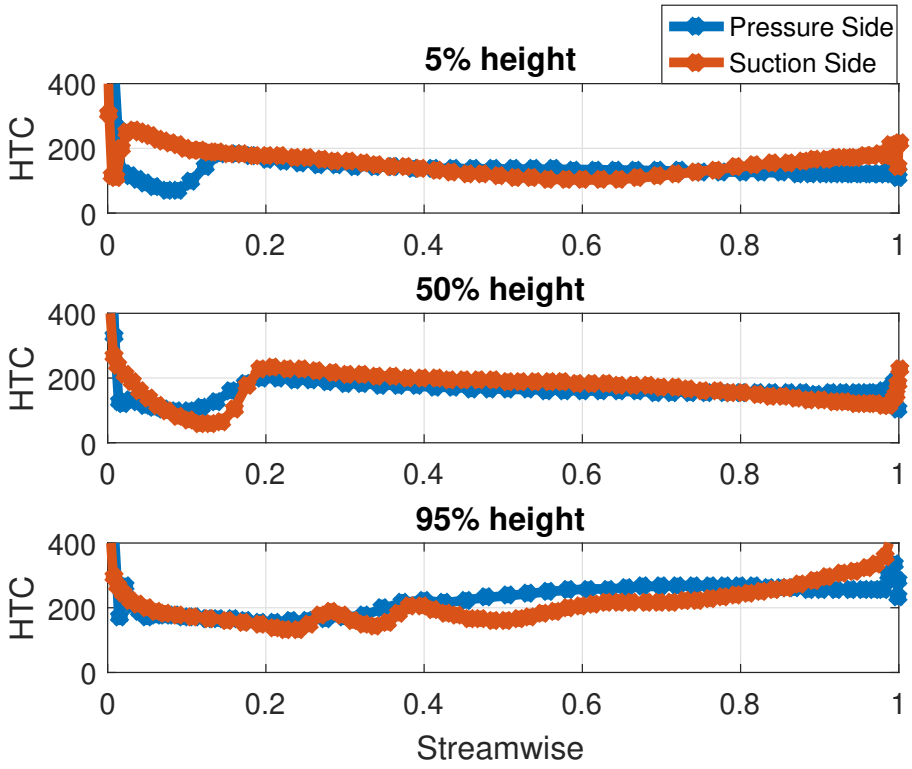

Figure 4.7: The heat transfer coefficient on suction and pressure side at different blade heights in cruise.

One can see how the transition is slower in the middle of the passage at 50% height, comparing to transition locations close to the end walls. The mid height and hub plots looks similar to what one would expect based on a flat plate case. Close to the shroud however, the flow to separates from the OGV surface. A vector plot of the velocity around the blade is shown in Figure 4.8.

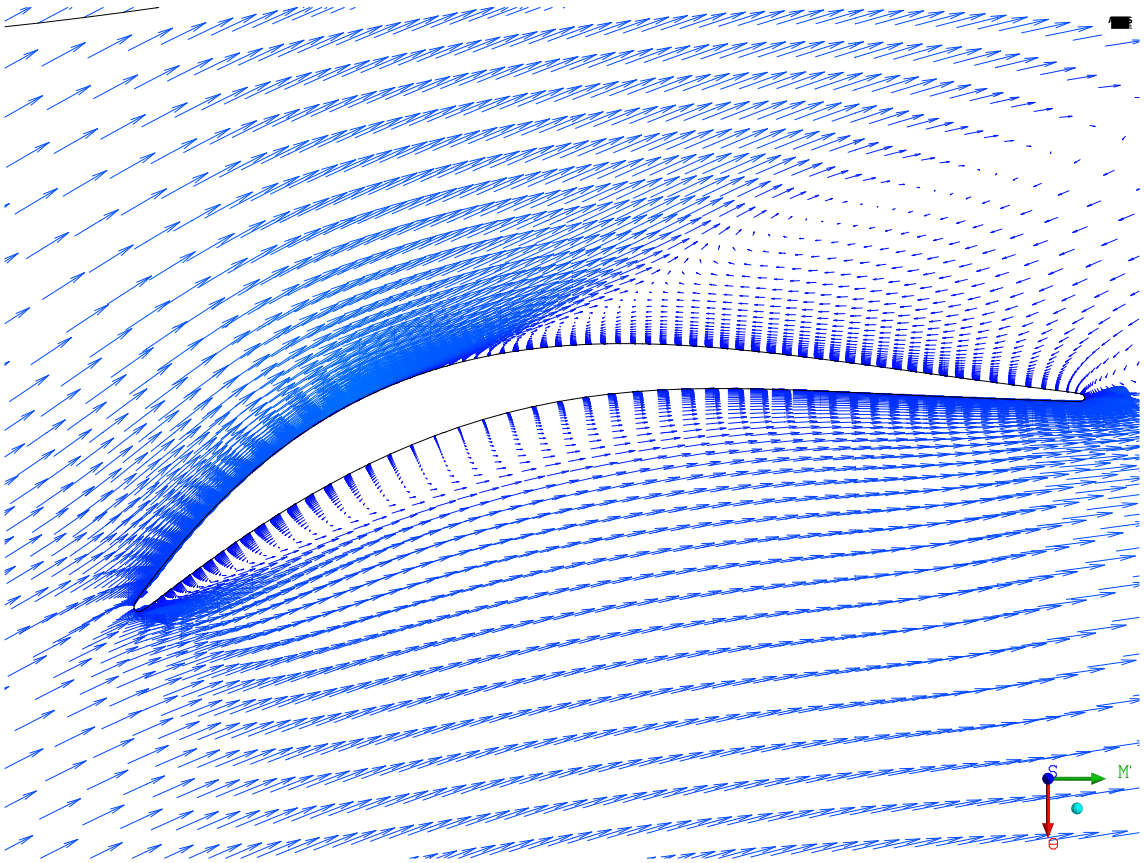

Figure 4.8: The velocity vector field close to the OGV blade at 95% of the height.

The flow on the suction side is seen to separate at 40%, causing a large recirculation region in the flow. One can see peaks in the HTC on the suction side at 40% where separation starts and collides with the recirculating air. Closer to the trailing edge, the flow moves almost perpendicular towards the blade surface, being forced to turn. Here, an increase in heat transfer coefficient is also seen, which might be attributed to this. This also explains why, in general, the pressure side has a slightly higher heat transfer coefficient, as the flow smashes into this surface, forcing it to turn.

The last interesting section of the heat transfer coefficient to discuss for this case is the leading edge on the pressure side. For the first 60% of the height, a small laminar region is present, that is abruptly changed to a peak in heat transfer coefficient. A velocity vector plot of this region can be seen in Figure 4.9. This is also caused by a small separation in the flow, causing multiple small whirls to appear, recirculating. This issue is caused by a negative incidence angle of the incoming flow, that can be fixed by slightly altering the shape of the OGV. Closer to the shroud, one large recirculation area is instead seen, as in figure 4.8.

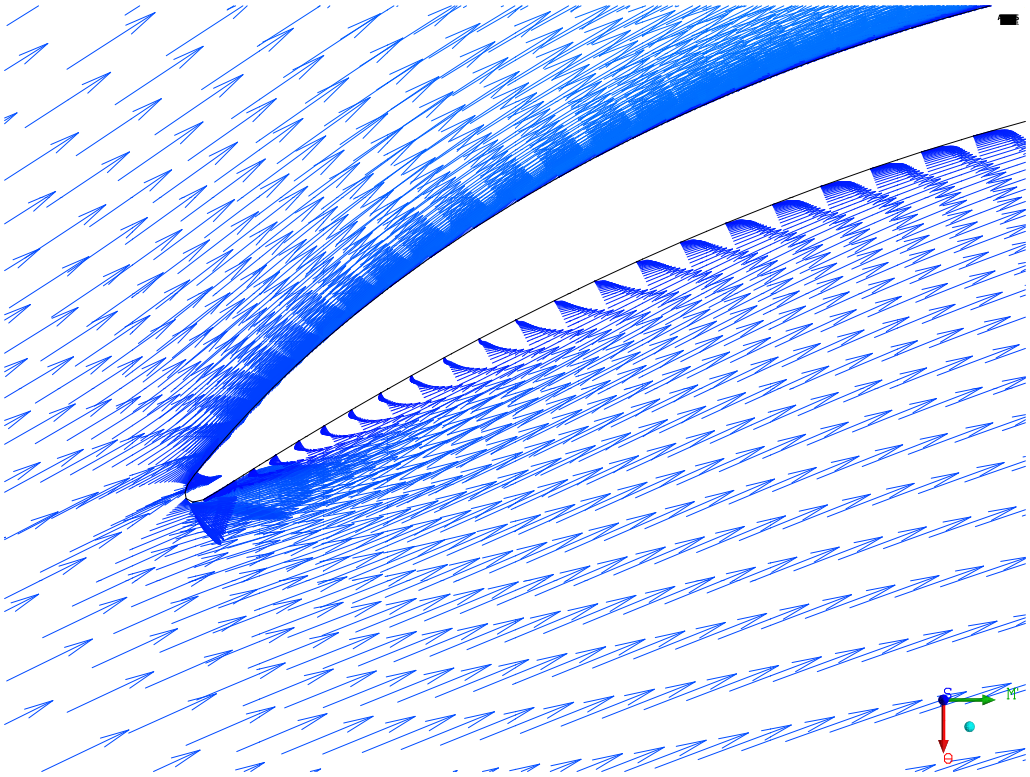

Figure 4.9: The velocity field at the leading edge of the OGV blade at 80% height.

4.1.5 Ground idle

The fan pressure ratio and efficiency map for the ground idle case is shown in Figure 4.10. Also shown in the reference point, which is established by assuming a surge margin of 16% similar to the cruise case. The reference point is used for all simulations in ground idle.

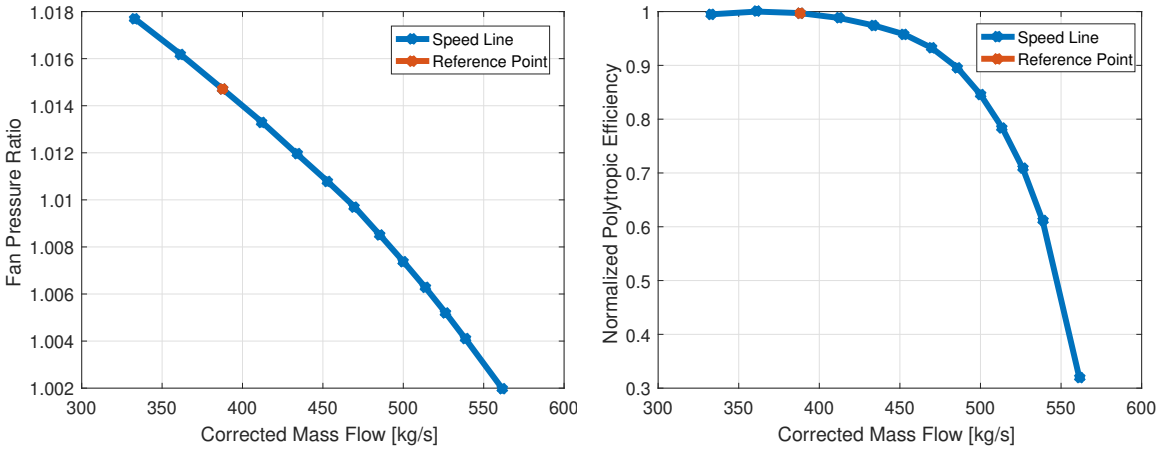

(a) Fan pressure ratio **(b)** Polytropic efficiency

Figure 4.10: Mapping of the ground idle case

4.1.5.1 Heat transfer coefficient

The heat transfer coefficient on the suction and pressure side of the OGV blade for the ground idle case is given in Figures 4.11 and 4.12. The suction side, compared to the cruise case, looks completely different. Instead of a relatively early transition to turbulence, one can see a low heat transfer coefficient on large portions of the blade, attributed to laminar flow. Furthermore, no large separations zone can be seen close to the shroud. On the pressure side, the cases share a similar appearance. On a large portion of the leading edge, the incidence angle of the flow is negative, causing small vorticies appear, increasing the heat transfer coefficient, similar to Figure 4.9 in cruise. The average heat transfer coefficient on the blade in ground idle is 142.3 W/m^2K. This is also seen in Figure 4.13, where the heat transfer coefficient distribution is shown along three heights, one close to the hub (5%), one close to the shroud (95%) and one in the middle (50%).

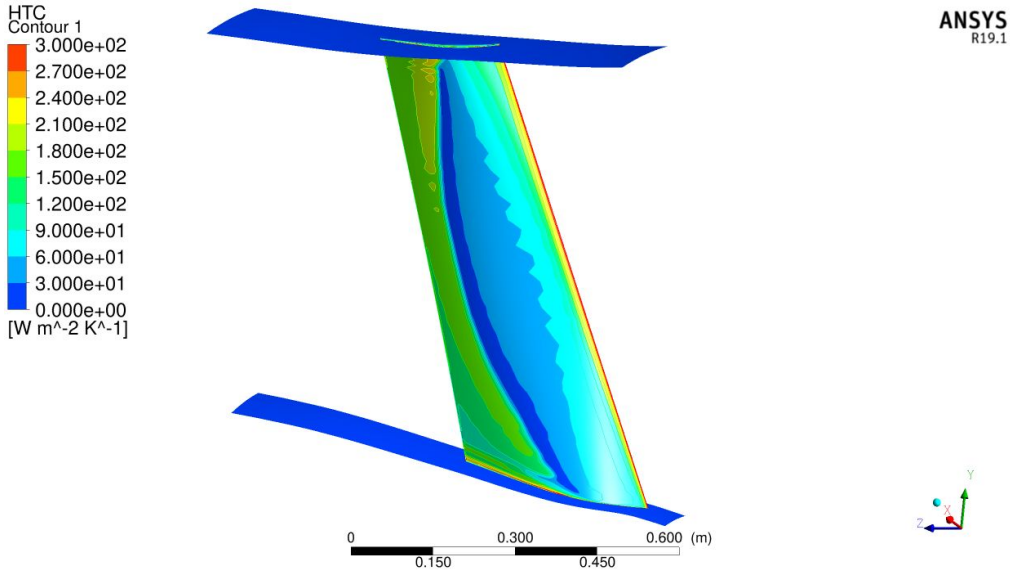

Figure 4.11: Heat transfer coefficient on the suction side of the OGV blade in ground idle.

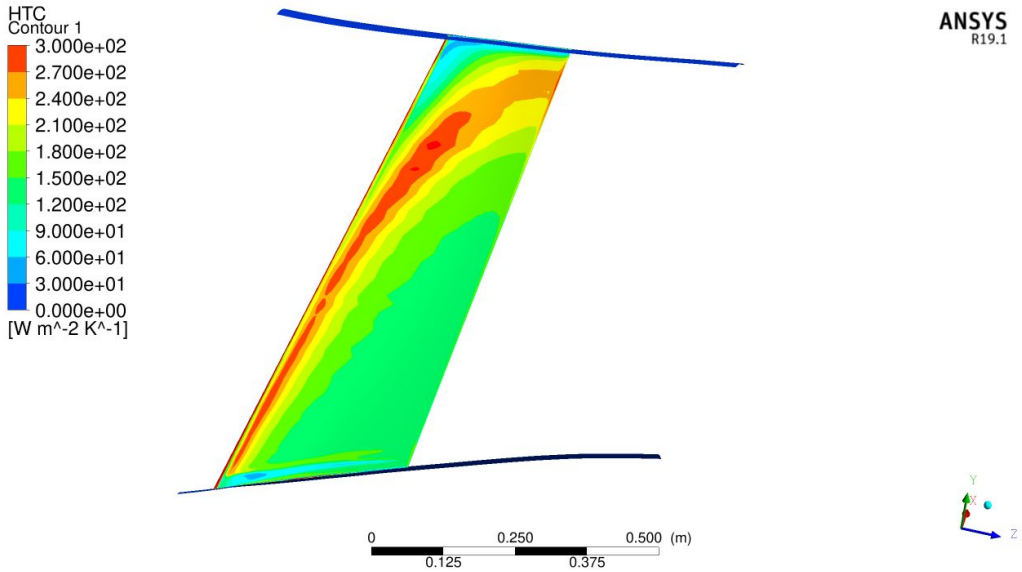

Figure 4.12: Heat transfer coefficient on the pressure side of the OGV blade in ground idle.

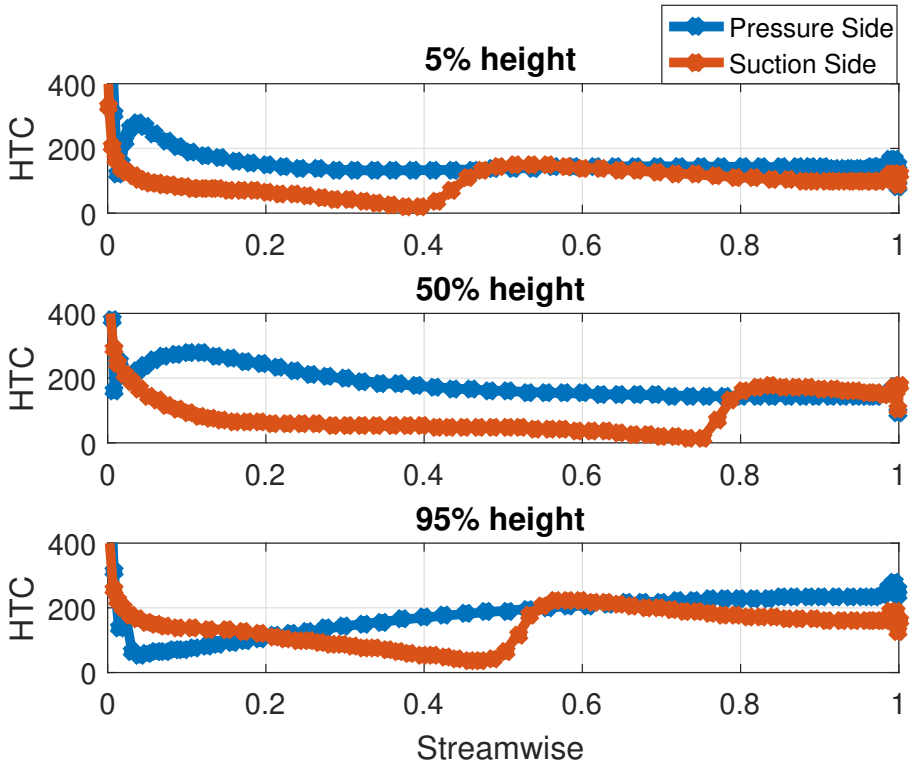

Figure 4.13: The heat transfer coefficient on suction and pressure side at different blade heights in ground idle.

4.1.6 Low aspect ratio OGV

The heat transfer coefficient on the low aspect ratio OGV in ground idle on the suction and pressure side can be seen in Figures 4.14 and 4.15. On the suction side, a similar trend to earlier can be seen, with a relatively large portion of the blade surface experiencing laminar flow, and thus having a low heat transfer coefficient. Further downstream the flow transitions to turbulent and the heat transfer coefficient increases. On the pressure side, the large HTC on the leading edge only appears close to the hub, decreasing radially. The rest of the surface is very uniform. The larger laminar area takes a toll on the average heat transfer coefficient, only reaching 116.106 W/m^{2}K. The blade area is 1.94 m^2, which is about 4 times as large as the regular OGV. For the full annulus, the total OGV area is slightly decreased, from 19.35 to 17.46m^2. This is also seen in Figure 4.16, where the heat transfer coefficient distribution is shown along three heights, one close to the hub (5%), one close to the shroud (95%) and one in the middle (50%).

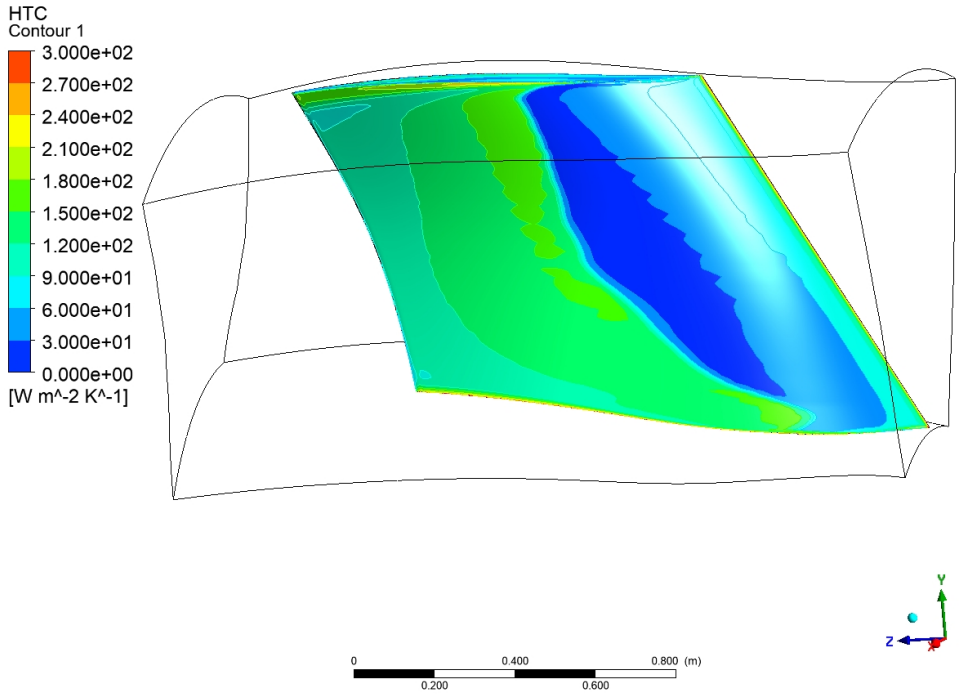

Figure 4.14: Heat transfer coefficient on the suction side of the low aspect ratio OGV blade in ground idle.

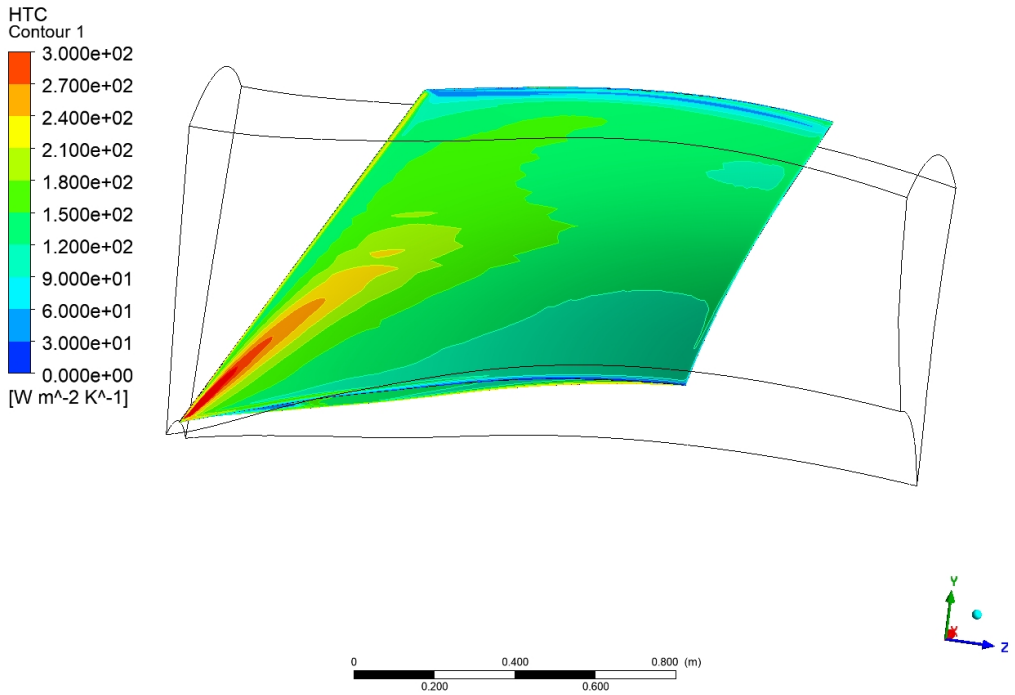

Figure 4.15: Heat transfer coefficient on the pressure side of the low aspect ratio OGV blade in ground idle.

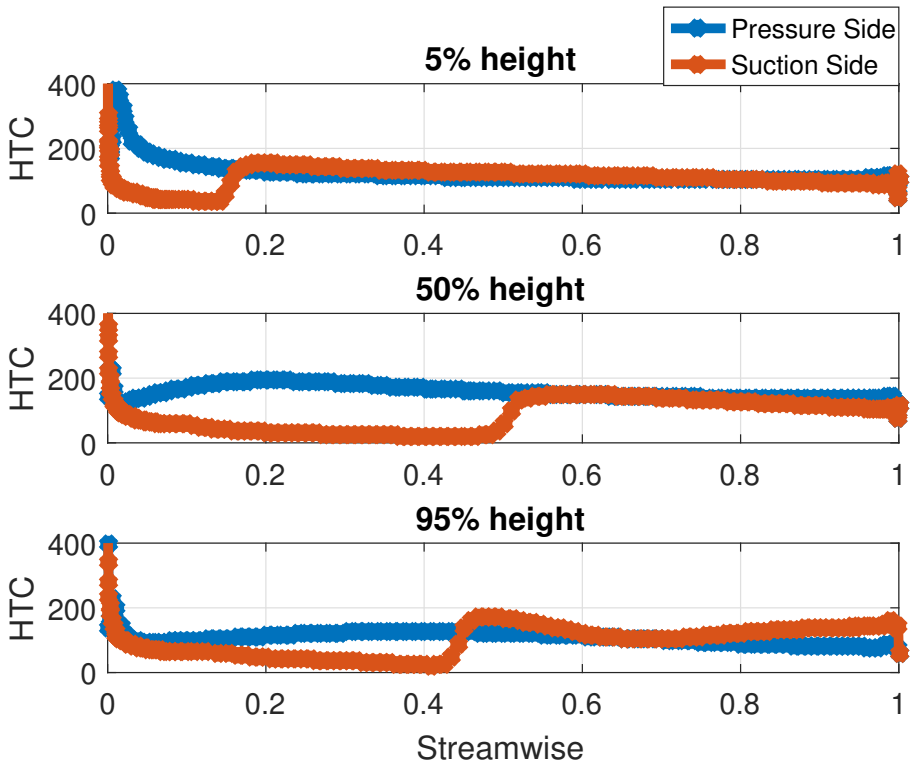

Figure 4.16: The heat transfer coefficient on suction and pressure side at different blade heights in ground idle for the low aspect ratio OGV.

4.2 Wall Resistance

In the following section, correlations used to calculate wall resistance are created, and the simulation model is validated by a mesh independence study.

4.2.1 Mesh independence study

To make sure that the data is valid, a small mesh independence study is carried out using 4 different meshes. Since geometry changes between each simulation, the element count varies, instead a fixed element size is used. These are shown in Table 4.2.

Mesh	Element size [mm]
Rough	1
Medium	0.6
Fine	0.3
Very Fine	0.1
Extremely Fine	0.05

Table 4.2: Cell sizes used for mesh independence study.

The parameter measured is the total heat flux over the upper wall, as this is directly proportional to the wall resistance. The result of this can be seen in Figure 4.17,

where the heat flux is plotted a percentage of the extremely fine mesh. Here it can be seen the variation is quite small and all meshes are within 1% of the final mesh. Mesh number 4, the very fine mesh, is chosen to be suitable for the simulations, as it is very close to the extremely fine mesh.

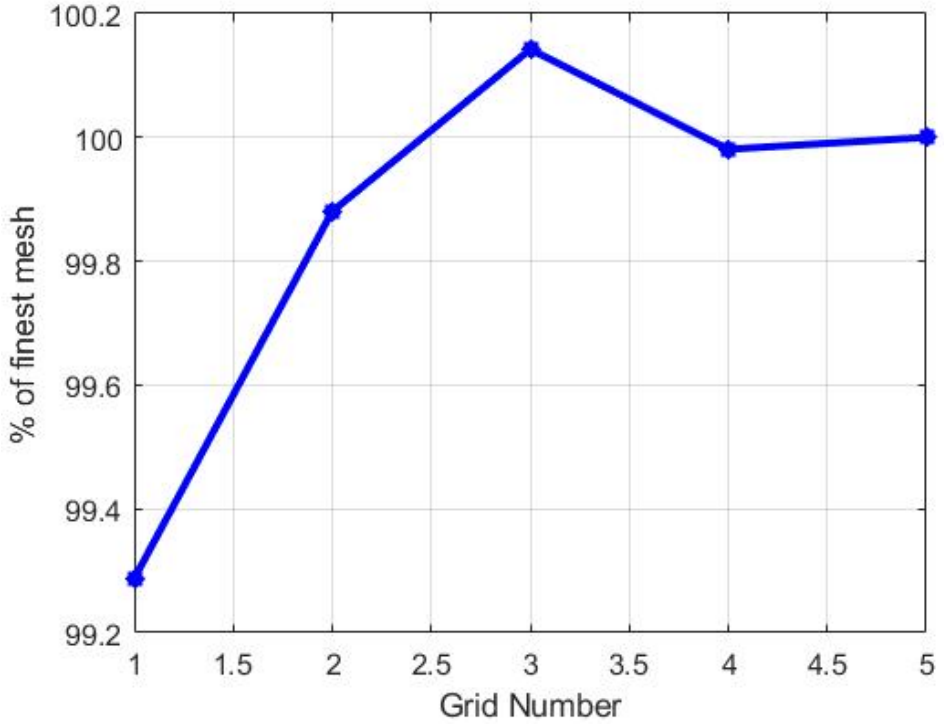

Figure 4.17: Mesh independence study of wall resistance as percentage of final solution

4.2.2 Wall resistance correlation

The test cases run for the parametrization of the wall resistance simulations are generated as a matrix by using all possible permutations in the range of the parameters. The desired results, in this case the heat flux over the surfaces, are given as an output vector for each case. The MATLAB curve fitting toolbox is used to correlate the input data with the results data. A figure of this tool is shown in Figure 4.18, with the results for the aluminium alloy. The blue points are generated by the simulations, and the surface is interpolated over the points.

As can be seen, the most influential parameter is the thickness ratio. For high thickness ratio we can see a very low wall resistance. This means that if the pipes are close to the surface, we see a higher heat transfer rate, which is expected. The length ratio only seems to have a large effect on the wall resistance when the thickness ratio is high, otherwise it is more or less constant. Judging from only the wall resistance perspective, it is always more beneficial to have thicker pipes, as the wall distance decreases. If the thickness ratio is low, it is more beneficial to have a distance longer between the pipes.

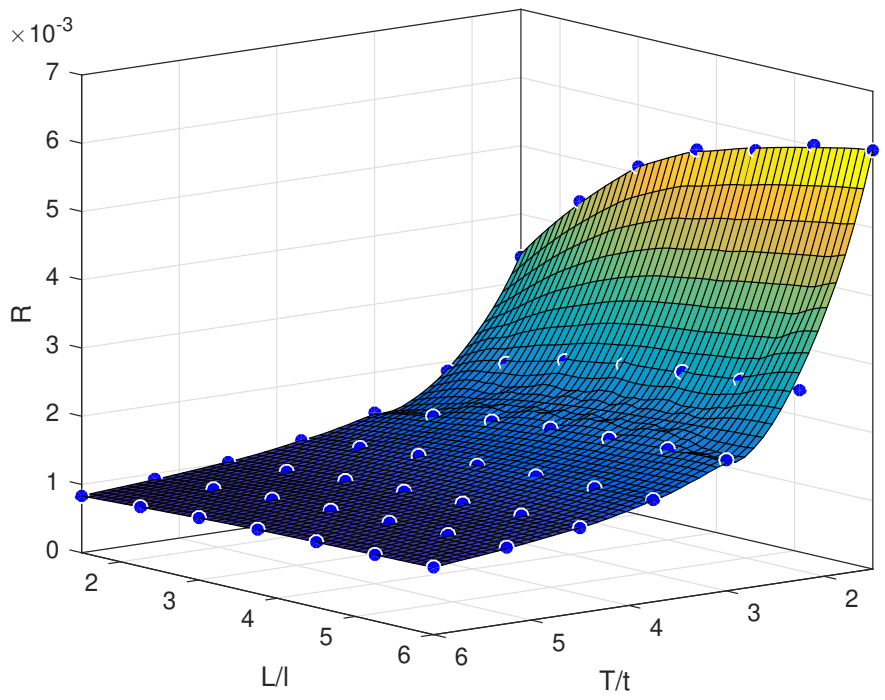

Figure 4.18: Curve fitting data for wall resistance using 2219 aluminium alloy

By examination of the data, it is decided that the dependency of length ratio is similar to that of a second degree polynomial function. The dependency on thickness ratio is similar to a power function. Furthermore, a linear dependence on the thermal conductivity of the material can also be seen in the difference between the two test cases. The difference in thermal conductivity for the materials is

$$\frac{k_{Al}}{k_{Ti}} = 19.8611 \tag{4.1}$$

while the difference in the simulation data is constant at

$$\alpha = 19.5865 \tag{4.2}$$

The correlation used to describe the wall resistance is given by equation 4.3. The shape of this equation is based on the reasoning above.

$$R = \alpha \left[a + b\left(\frac{L}{l}\right) + c\left(\frac{L}{l}\right)^2 \right] \left[\left(\frac{T}{t}\right)^d + \left(\frac{T}{t}\right)^e + f \right] \tag{4.3}$$

where α is 1 for aluminium and 19.5865 for titanium, and a - f are constants determined by the curve fitting tool. These are given as

$$\begin{bmatrix} a \\ b \\ c \\ d \\ e \\ f \end{bmatrix} = \begin{bmatrix} 0.004525 \\ 0.003426 \\ -0.0002977 \\ -3.205 \\ -0.05665 \\ -0.8341 \end{bmatrix} \tag{4.4}$$

The goodness of the fit are measured by the following values.

- The sum of squares due to error (SSE): 5.05e-07
- R-square: 0.9951
- Adjusted R-square: 0.9945
- Root mean squared error (RMSE): 0.0001084

As an exact fit gives a R-square and adjusted R-square of 1, and a SSE and RMSE of 0, it is deemed that this fit is close enough, and used in further calculations of wall resistance.

4.3 Cooling System

A simplified version of the system architecture of the cooling system code is shown in Figure 4.19. The program takes as input: the first pipe location; the number of pipe passes; the distance between pipes; and the coolant. The outputs are the heat rejected from the OGV, as well as the predicted pressure losses in all pipes.

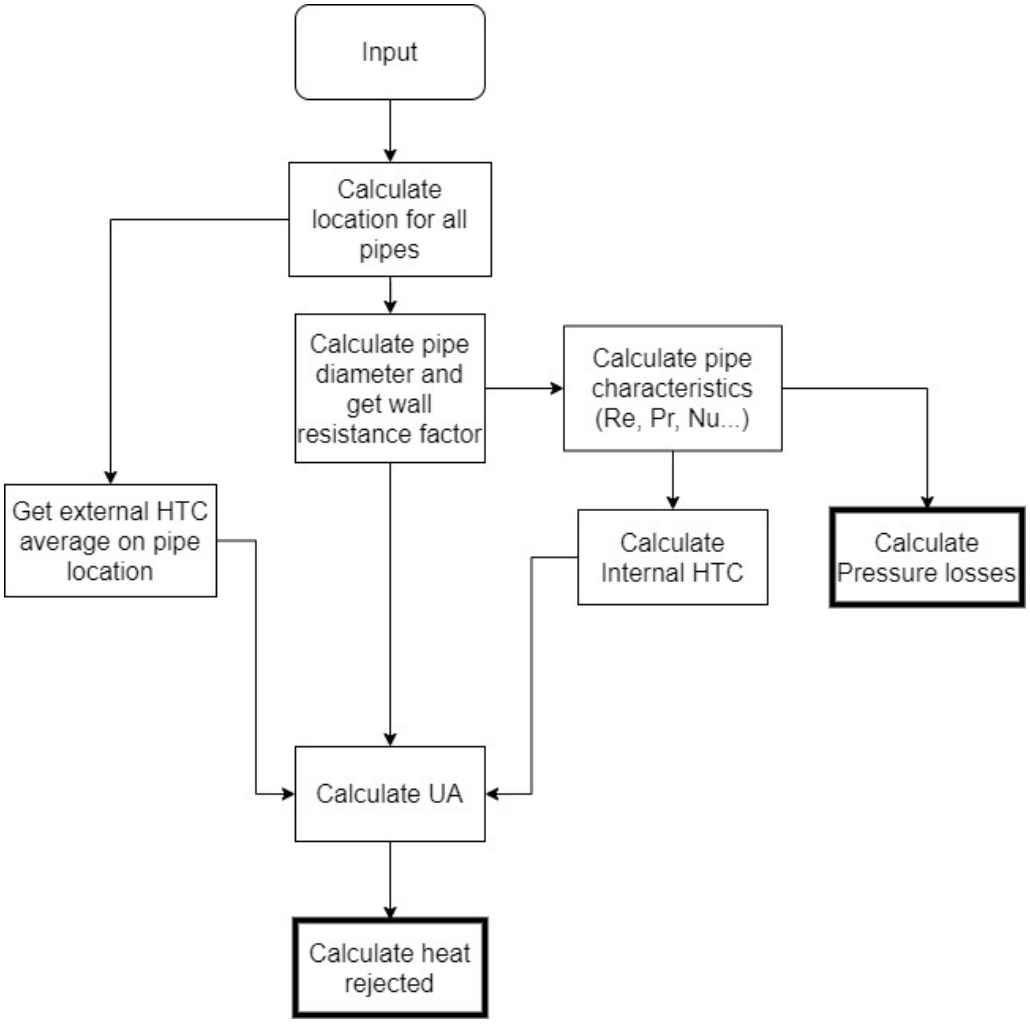

Figure 4.19: Cooling system code flow shart.

4.3.1 Optimization

The code above is used as the minimization function in the optimization code, along with some constraints on the input variables. The constraints are as follows

- First pipe location between 5.7% and 76.7% of the span. The leading edge constrain is based on a minimum allowed diameter of the first pipe, set to 0.5 cm, while the trailing edge is chosen arbitrarily as no solution with only pipes at the trailing edge only is expected.
- The number of pipe passes are between 2 and 14, based on the maximum amount of pipes that can be fitted inside the OGV.
- The distance between pipes are set between 2 and 7 centimeters, this ensures that it is within the span of the wall resistance correlation.
- The coolant parameter varies from 1 to 10. This is used to select the desired coolant in a predefined matrix where each row is a different coolant, outputting density, viscosity, heat capacity, and heat conduction coefficient.

It should be noted that these constraints are altered for the low aspect ratio OGV, as for example the thicker blade allows for pipes closer to the leading edge, and much thicker pipes. These constraints are

- first pipe location is between 0.74% and 81.4% of the span. Similar to before the leading edge is based on a minimum pipe diameter while the trailing edge is set arbitrarily.
- The number of pipe passes is set between 2 and 12.
- The distance between the pipes 11 and 35 cm, to be within span of the wall resistance correlation, as the pipe diameters are much larger in this case.
- The cooling parameter is identical to above.

4.3.2 OGV cooling performance

The genetic algorithm optimization is run using a population 300 individuals, for a minimum of 100 generations. For the ground idle case, the final generation can be seen in Figure 4.20. Instead of pressure drop, the pump power needed to overcome the pressure drop is given. Both the heat rejected and the pumping power is measured in the full annulus, assuming that all 43 OGV blades are used as heat sinks. All following results are presented for the case with 2219 aluminium alloy OGV, and a comparison to titanium Ti6Al4V is presented last.

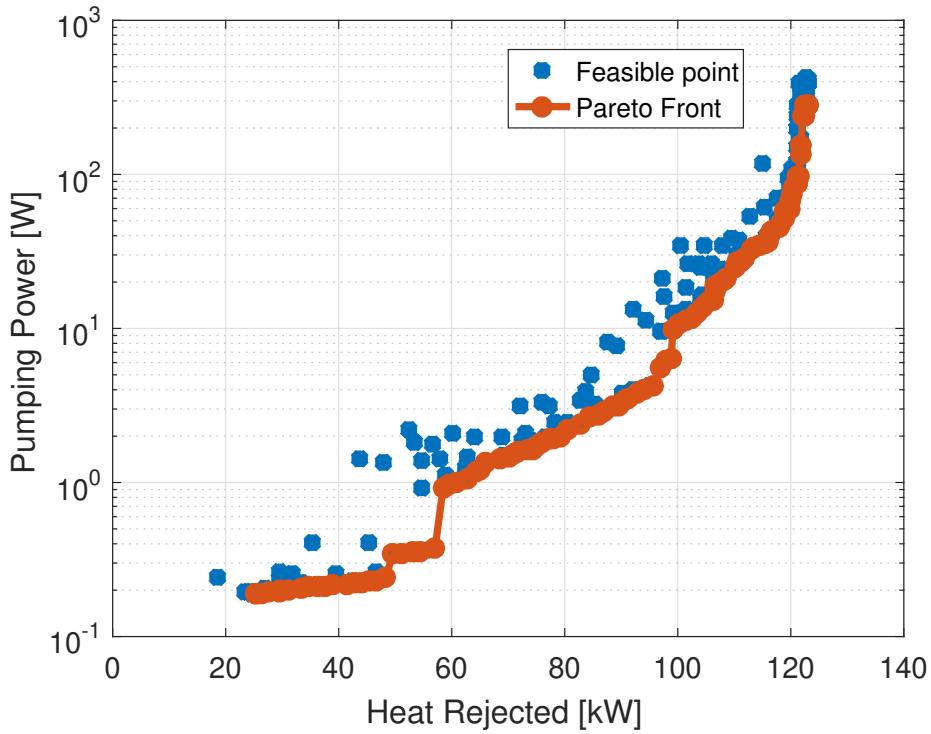

Figure 4.20: The final generation of the optimization for 2219 aluminium alloy.

4.3.2.1 Cooling system configurations

In the final generation of solutions, clear trends can be seen in the 105 individuals that make up the Pareto front. Most of the individuals can be categorized in one of three configurations. The three configurations are divided based on the number of pipe passes included. The Pareto front with the three configurations color coded is shown in Figure 4.21. Additionally, four points of interest are marked, where discontinuities are found.

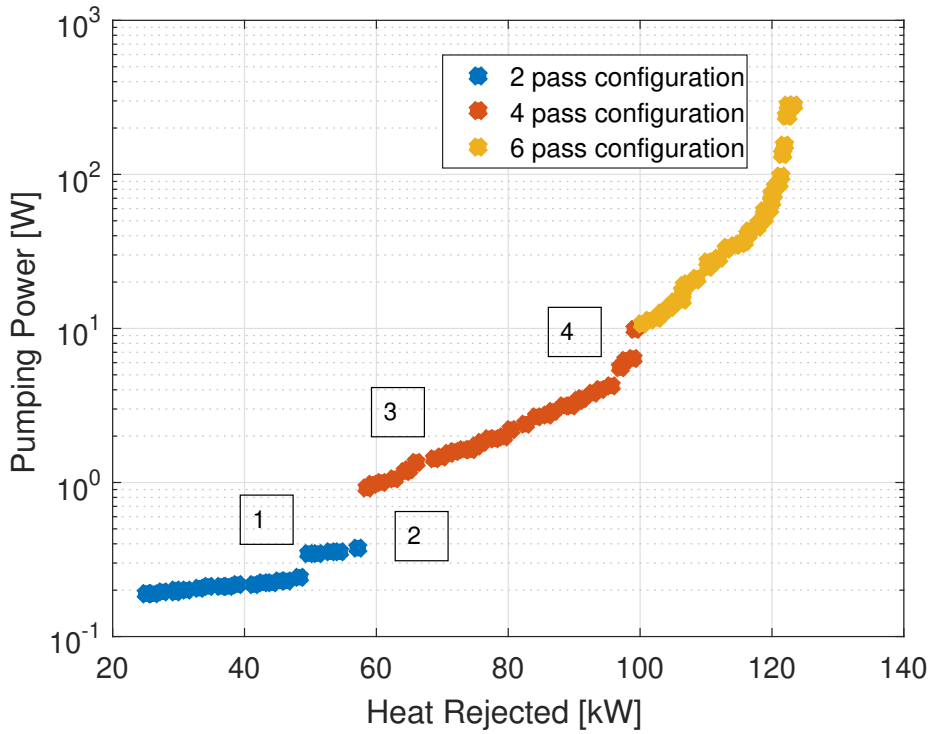

Figure 4.21: The three configurations from the optimization.

The coolants used in all configurations are Therminol D12 and 50% ethylene glycol, with Therminol D12 being dominant on the lower side of the spectrum while 50% ethylene glycol taking up the upper and middle part of the spectrum. The properties of these two coolants are compared in Table 4.3.

Property	Therminol D12	50% Ethylene Glycol
Density [kg/m^3]	706.8084	1028.0
Heat Capacity [kJ/K]	1.0280	3.4888
Viscosity [mPa· s]	43.432	93.998
Thermal Conductivity[W/m·K]	0.0975	0.3562

Table 4.3: The two coolants used by the Pareto optimal solutions.

It is clear that when a small pressure loss is sought, a coolant with lower viscosity and density is more favourable. At a certain point however, a maximum heat rejection is achieved using this coolant, and a coolant with better heat capacity and thermal conductivity is needed to achieve higher heat rejection. This comes at the cost of increased pressure drop. This can be seen above in Figure 4.21, where the sudden jump in pumping power on point 1. Some individuals in the 4 pass configurations also uses Therminol D12, but the pumping power jump here (point 3) is less apparent because an increase in heat rejection is also seen. This could be interpreted that a coolant with overall higher properties can be utilized better with more passes involved. At points 2 and 4, the number of passes increase to 4 and 6, respectively. In addition the first pipe location, and thus the pipe diameter changes drastically

here. The reason a single individual of the 4 pass configuration is located above the jump is because the location of the first pipe is very close to the leading edge, causing the first pipe diameter to be very small.

In Figure 4.22 the location of the first pipe is shown. As can be seen here, the three configurations behave quite differently here, with the 2 and 6 pass configurations being relatively uniform in first pipe placement, while the 4 pass configurations acts as a bridge between the two. With only two pipe passes, it is preferred to have them closer to the middle, since the thickness of the OGV is largest here, thus allowing larger pipe diameters that cause low pressure losses. When the number of pipe passes are increased, the location of the first pipe is pushed forward to allow for more pipes. The entirety of the 6 pass configuration is located very close to the leading edge, seeing as the closest allowable value is around 5.7%.

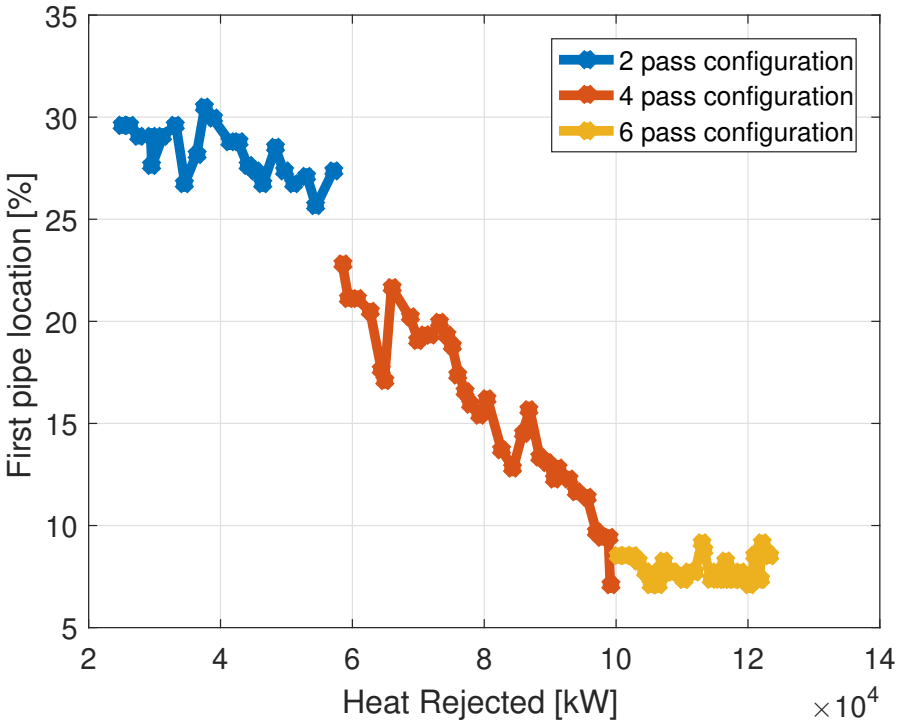

Figure 4.22: First pipe location in percentage of span

Furthermore, one can look at how the distance between the pipes change, this can be seen in Figure 4.23. Here it is seen that in all three configurations, the low end solutions prefer a small distance between the pipes. As the distance between the pipes increase, both pressure drop and heat rejection increases. The two discontinuities seen in the 2 and 4 pipes configurations can be attributed to change in coolant from Therminol D12 to 50% ethylene gylcol. The reason for the heat rejection and pressure drop increase with increasing distance can likely be attributed to the fact that with a higher distance, a larger portion of the OGV can be used as a heat sink, furthermore with larger distance between the pipes, the thickness of the pipes decrease as they are further from the thickest region. Smaller pipes cause a higher

pressure drop and an increase in internal heat transfer coefficient, further increasing heat rejected.

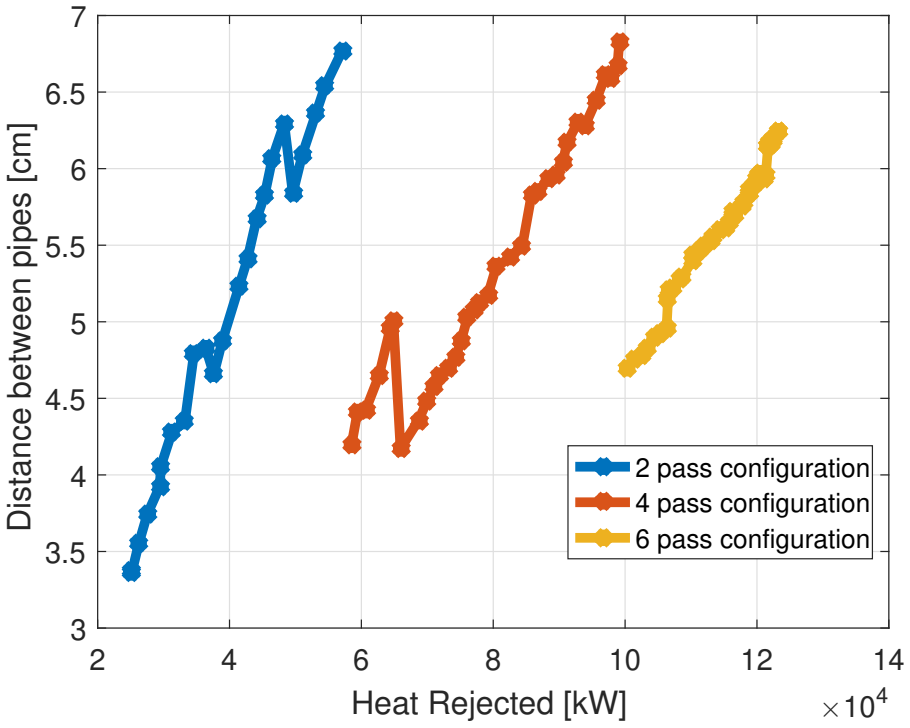

Figure 4.23: The distance between the pipes.

By measuring the components of heat transfer coefficient and pressure drop, one can find the key parameters deciding the performance of the system. The components of the heat transfer coefficient is shown in Figure 4.24, for each of the 105 individuals, ranked in terms of heat rejection, meaning individual 1 will have lowest heat rejected and individual 105 the highest. Keep in mind that heat transfer coefficient is calculated as

$$\frac{1}{UA} = \frac{1}{h_o A_o} + R_{wall} + \frac{1}{h_i A_i} \tag{4.5}$$

and as such, the lowest contribution will limit the overall heat transfer coefficient.

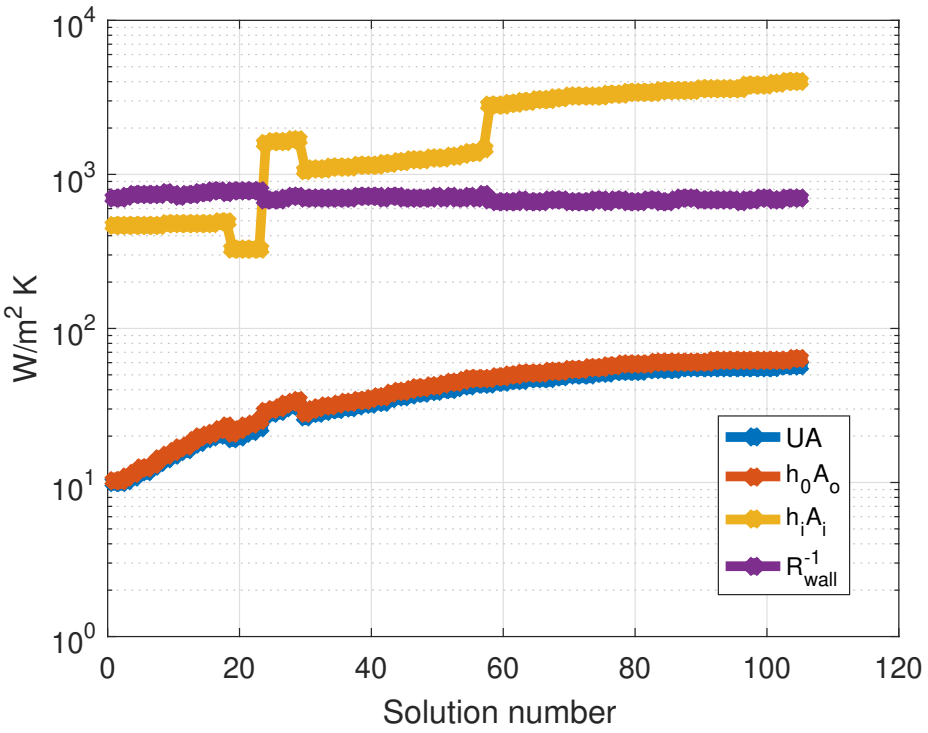

Figure 4.24: The components of the heat transfer coefficients for all the Pareto optimal solutions.

From this, it is quite clear that the limiting factor for heat transfer is the external heat transfer coefficient. As higher heat rejection is sought, the heat transfer surface is increased by increasing the distance between the pipes, and adding more pipes. The two discontinuities seen (point 1 and 2) are caused by the change in coolant. As mentioned before, when the coolant changes the distance between the pipes drop, and as such, the area of the OGV covered by the pipes decrease, decreasing the overall heat transfer coefficient. The heat rejection, however, is also a factor of what coolant is used, and therefore the heat rejection is still increased even though the overall heat transfer coefficient decreases. A similar figure for pump work contributions is shown in Figure 4.25. The total pump work is simply the sum of the components.

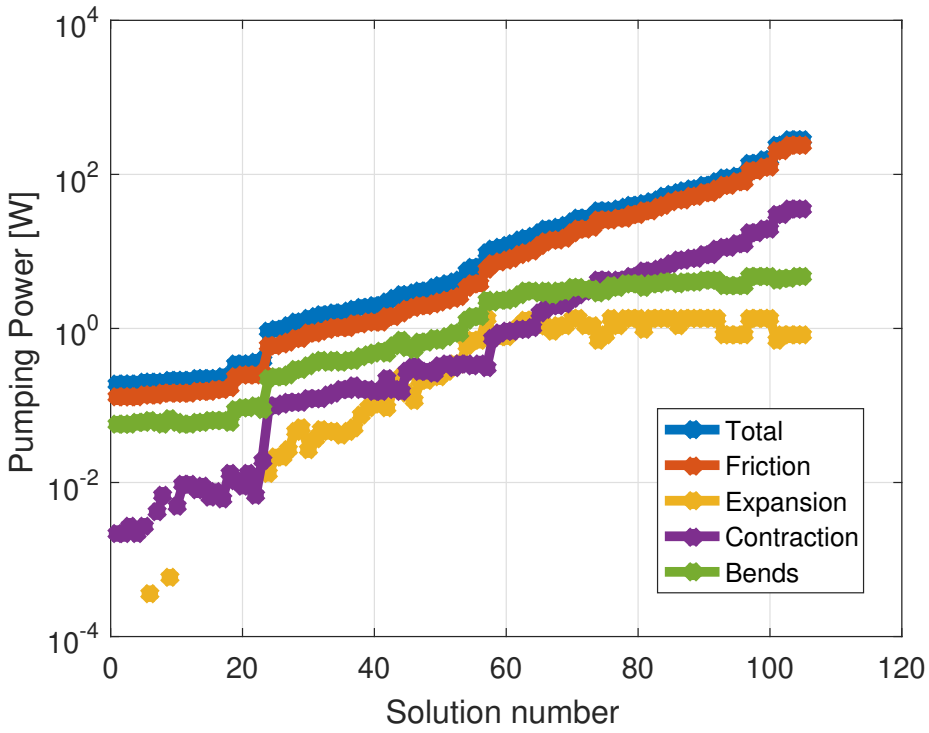

Figure 4.25: The contributions to the pumping power or all the Pareto optimal solutions.

Here we can see that the majority of the losses comes from frictional losses, with the second most important arguably being from bends in the pipes. The losses from expansion and contraction becomes more important as the number of pipe passes increase to 4 and 6, which is not very surprising.

4.3.2.2 Cooling performance for titanium alloy

In Figure 4.26, the Pareto front of the OGV using the titanium alloy Ti6Al4V is shown. The settings are identical to the earlier presented case. As can be seen, the shape of the result look very similar to the results presented in Figure 4.20. In the lower end of solutions, the increased wall resistance of the titanium is not a major factor, and similar values of heat rejection can be seen for aluminium and titanium. As heat transfer increase it can be seen that the wall resistance is limiting the increase in heat rejection quite substantially, as maximum values only reach about 60 kW, compared to earlier 120 kW. The trends in the piping system are very similar to the previous section, the only exception being a higher preference of only 2 pipes, as an increase in number of pipe passes does not give a large increase in heat transfer because of the limiting wall resistance.

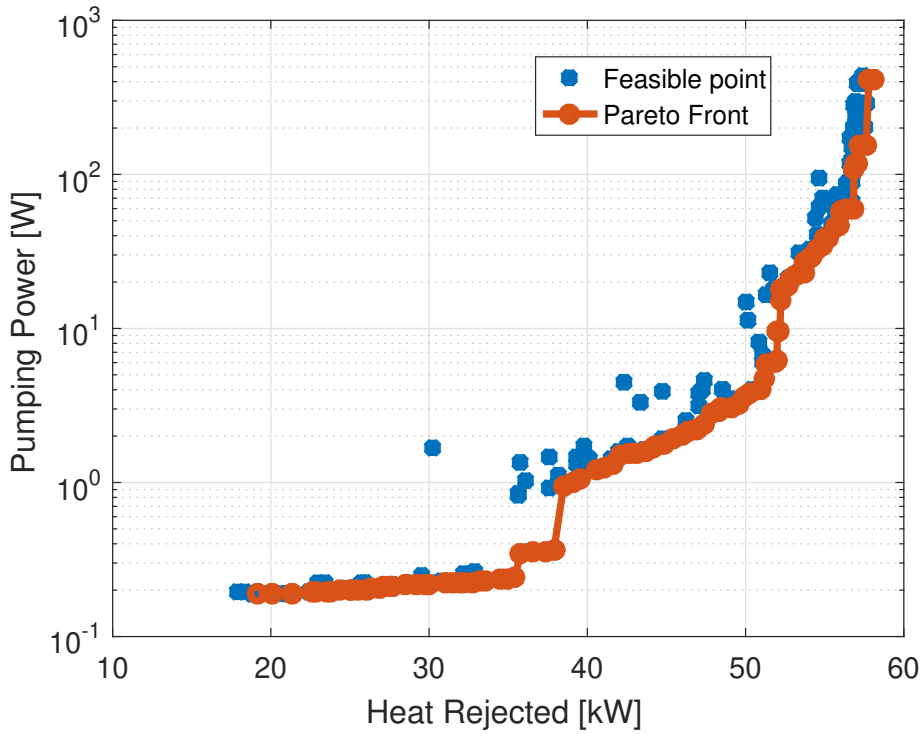

Figure 4.26: Pareto front for the idle case using an Titanium OGV.

4.3.2.3 Cooling performance in cruise

The cooling system code is run using all the 105 optimal solutions in the Pareto front for the ground idle case. The result of this is shown in Figure 4.27. The results look very similar to the earlier shown results, only the heat rejected seeing an increase. This is to be expected since the overall heat transfer coefficient of the OGV blade and the mass flow is larger. It is probable that this is not the optimal configurations of pipes, as the heat transfer coefficient distribution is quite different in the two cases, but nevertheless, it still gets the job done.

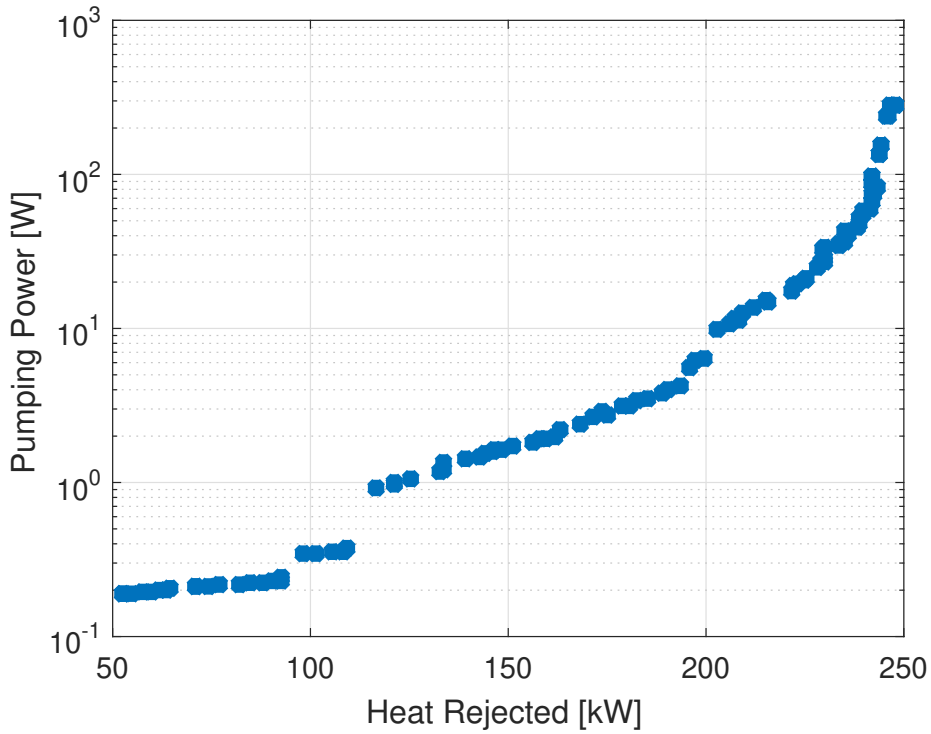

Figure 4.27: The Pareto optimal solutions for ground idle in cruise.

4.3.3 Low aspect ratio OGV cooling performance

In Figure 4.28, the Pareto front for the low aspect ratio OGV in ground idle can be seen. This case is only run with a population of 300 individuals. As can be seen, the largest difference in performance is a much reduced pumping power. This can be attributed to substantially thicker pipes, slowing down the velocity of the coolant, and thus reducing losses. In the regular OGV, the thickest pipes located at 30% of the span have a diameter of about 1.25 centimeters, while in this case pipe diameters can be 7 cm. The heat rejection is comparable, being a bit higher in the low aspect ratio OGV.

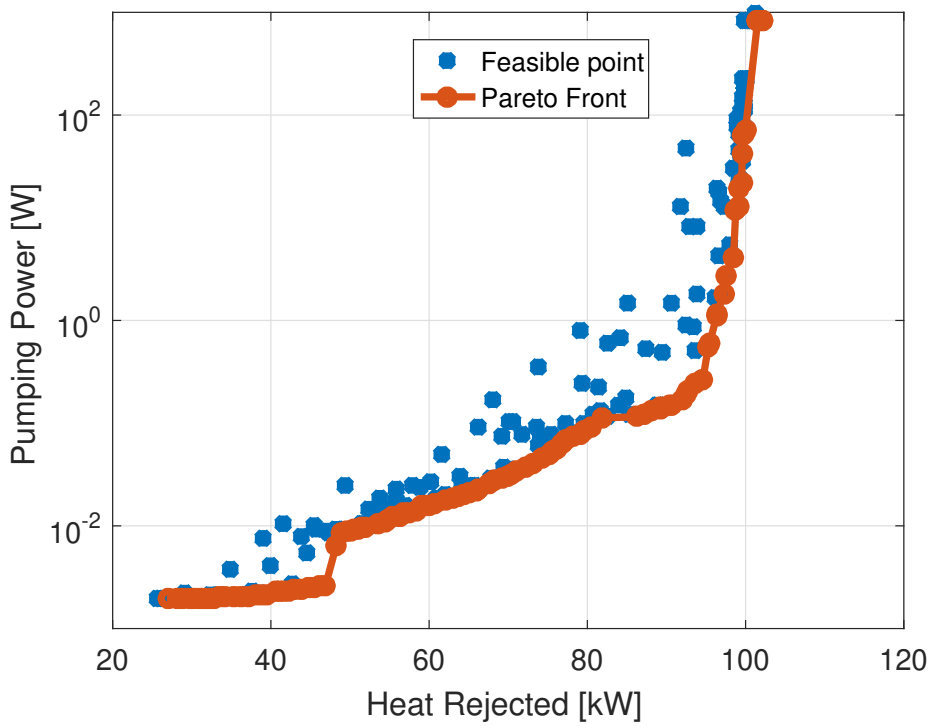

Figure 4.28: Pareto front for low aspect ratio OGV in ground idle.

Overall, the results from this blade follow the same trends presented earlier. The first pipe location starts at around 35% of the span, moving closer to the leading edge as higher heat rejection is required. The solutions closest to the leading edge are at around 5% of span. The number of pipe passes also starts low, at two pipes, increasing as heat rejection increases up to four and then six. A few solutions in the high end of heat rejection even uses eight pipes. The coolant distribution is identical, with low end solutions preferring Therminol D12, switching to 50% Ethylene Gycol as required. The distance between the pipes also follows the clear trend from before, increasing to increase heat rejection. The distance varies between 13 to 34 centimeters.

5
Conclusion

5.1 Cooling system summary

Based on the results obtained, several different cooling systems configurations look From on the results obtained, the optimal cooling system to implement based on the optimization results for the idle case is a member of the first family. This means a piping system with only 2 pipes going through the OGV. To keep a relatively high safety margin, a solution achieving around 50kW of heat rejection might be suitable. This is based on the fact that the idle case mass flow was quite a bit higher than the predictable values and might be subject to change. In case of lower mass flow, this piping system should still be sufficient to reach 20kW of heat rejection. The chosen specifications is given in table 5.1.

Property	value
First pipe % of span	25.93
Number of pipes	2
Coolant	Therminol D12
Distance between pipes	6.52 cm

Table 5.1: The specifications of the chosen cooling configuration.

Worth discussing is also the fact that running pipes though the OGV would reduce their stiffness, which might be an issue. In this case, a possible option is to have a pipe configuration that achieves higher heat rejection, but only using say half or one third of the OGV as heat exchangers, leaving the rest to take up a majority of the structural load.

5.2 Margins of error

As different methods are used to estimate the different parts, of the heat transfer problem, the results will depend on the lowest fidelity methods used. In this case, the CFD RANS simulations are of highest fidelity, while the wall resistance and pipe correlations are lower. Because of this, higher margins of error should be expected in these results. These fidelity issues could perhaps be solved by doing a simulation of the heat exchanger system, using the heat transfer coefficient on the OGV surface as boundary condition, and running pipes though it. As these simulations would be more lengthy, an optimization using this method would likely be too time consuming,

and the results presented in this thesis could be used as a starting guess. This type of simulation would provide more accurate results not only in terms of heat rejection, but also in the pipe pressure drop. The OGV blade profiles used in this thesis are not final, which is why large separation zones and negative incidence angles are seen in some of the results. Both these factors increase the heat transfer coefficient, and thus the heat rejection. From an aerodynamic point of view however, these are negative, and will likely be fixed in future iterations of the engine.

Bibliography

[1] Davidson, L (2021) *Fluid mechanics, turbulent flow and turbulence modeling*

[2] Davidson, L (2018) *An Introduction to Turbulence Models*

[3] ANSYS, Inc (2009) *ANSYS CFX - Solver Theory Guide*

[4] ANSYS, Inc (2021) *ANSYS CFX - Solver Modelling Guide*

[5] Saravanamuttoo, H.I.H. Cohen, H. Rogers, G.F.C. (2001) *Gas Turbine Theory*, Pearson Education, Ltd.

[6] CFD-online (2005) *Favre averaged Navier-Stokes equations*, viewed 3 May 2021, `https://www.cfd-online.com/Wiki/Favre_averaged_Navier-Stokes_equations`

[7] Dixon, S.L. Hall, C.A. (2014) *Fluid Mechanics and Thermodynamics of Turbomachinery*, Elsevier Inc.

[8] Graver, B. Zhang, K. Rutherford, D. (2019) *CO2 emissions from commercial aviation, 2018*, ICCT

[9] Mazareanu, E. (2021) *Number of flights performed by the global airline industry from 2004 to 2021*, Statista

[10] Bergman T.L, Lavine A.S, Incropera F.P, Dewitt D.P (2011) *Fundamentals of Heat and Mass Transfer*, John Wiley and Sons

[11] Cengel Y.A, Cimbala J.M, Turner R.H (2017)*Fundamentals of Thermal-Fluid Sciences*, McGraw-Hill Education

[12] White F.M. (2011) *Fluid Mechanics*, The McGraw-Hill Companies, Inc.

[13] W.M. Kays, A.L. London (1964) Compact Heat Exchangers, The McGraw-Hill, Inc.

[14] John H. Lienhard V (2020) *Heat Transfer in Flat-Plate Boundary Layers: A Correlation for Laminar, Transitional, and Turbulent flow*, ASME, Journal of Heat Transfer

[15] Menter, F. R. (1993) *Zonal Two Equation k-w Turbulence Models For Aerodynamic Flows*, AIAA Paper 93-2906.

[16] Wilcox, D. C. (1988) *Reassessment of the Scale-Determining Equation for Advanced Turbulence Models*, AIAA Journal, Vol. 26, No. 11, 1988, pp. 1299-1310.

[17] Jones, W. P. Launder, B. E. (1972) *The Prediction of Laminarization with a Two-Equation Model of Turbulence*, International Journal of Heat and Mass Transfer, vol. 15, 1972, pp. 301-314.

[18] Menter, F. R. Langtry, R. and Volker, S. (2006) Transition Modelling for General Purpose CFD Codes, Flow, Turbulence and Combustion, Vol. 77, No. 1, Nov. 2006, pp. 277-303.

[19] Mayle, R.E. (1991) The Role of Laminar-Turbulent Transition in Gas Turbine Engines, ASME Journal of Turbomachinery, Vol. 113, pp. 509-537, 1991.

[20] Lejon, M. (2018) *Aerodynamic design framework for low-pressure compression systems*, PhD thesis, Chalmers University of Technology, Gothenburg

[21] Kader, B.A. (1981) *Temperature and concentration profiles in fully turbulent boundary layers*, International Journal of Heat and Mass Transfer, 24(9):1541-1544, 1981.

[22] Seresinhe, R. (2014)*Impact of aircraft systems within aircraft operation: A MEA trajectory optimisation study*, PhD thesis, Cranfield University, Cranfield

[23] Andersson, F. (2018) *Integrated generator for use in aircraft engines*, Lunds Universitet, Lund

[24] Jafari, S. Nikolaidis, T. (2018) *Thermal Management Systems for Civil Aircraft Engines: Review, Challenges and Exploring the Future*, Cranfield University, Cranfield

A

Appendix

A.1 Boundary Conditions - Flat plate

Boundary conditions	Cruise	Ground idle	Unit
Inlet total pressure	52507	102884	[Pa]
Inlet total temperature	276.639	329.662	[K]
Turbulent intensity	5	5	[%]
Outlet pressure(static)	40000	100000.65	[Pa]
Wall temperature	373	373	[K]

Table A.1: Data for flat plate boundary condition in cruise and idle.

A.2 Boundary Conditions - Fan simulations

	Cruise	Ground idle	Unit
Altitude	35000	0	[ft]
Aircraft Mach	0.84	0	[-]
Total temperature	249.7778	328.150	[K]
Total pressure	37507.5	101315	[Pa]
BPR	13.9	15.81	[-]
Mass Flow	570.57	-	[kg/s]
Fan Rot. Speed	-	520	[rpm]
Fan PRTT	1.391	-	[-]

Table A.2: Data for operating conditions of the engine.

DEPARTMENT OF MECHANICS AND MARITIME SCIENCE
CHALMERS UNIVERSITY OF TECHNOLOGY
Gothenburg, Sweden
www.chalmers.se

CHALMERS
UNIVERSITY OF TECHNOLOGY